The interstellar medium of dwarf galaxies: new insights from Machine Learning analysis of emission line spectra

G. Ucci[1]★, A. Ferrara[1,2], S. Gallerani[1], A. Pallottini[1,3,4,5], G. Cresci[6],
C. Kehrig[7], L. K. Hunt[6], J. M. Vilchez[7], L. Vanzi[8]

[1] *Scuola Normale Superiore, Piazza dei Cavalieri 7, 56126, Pisa, Italy*
[2] *Kavli IPMU, The University of Tokyo, 5-1-5 Kashiwanoha, Kashiwa 277-8583, Japan*
[3] *Centro Fermi, Museo Storico della Fisica e Centro Studi e Ricerche "Enrico Fermi", Piazza del Viminale 1, Roma, 00184, Italy*
[4] *Cavendish Laboratory, University of Cambridge, 19 J. J. Thomson Ave., Cambridge CB3 0HE, United Kingdom*
[5] *Kavli Institute for Cosmology, University of Cambridge, Madingley Road, Cambridge CB3 0HA, UK*
[6] *INAF - Osservatorio Astrofisco di Arcetri, largo E. Fermi 5, 50127 Firenze, Italy*
[7] *Instituto de Astrofísica de Andalucía, CSIC, Apartado de correos 3004, 18080 Granada, Spain*
[8] *Department of Electrical Engineering and Center of Astro Engineering, Pontificia Universidad Catolica de Chile,*
Av. Vicua Mackenna 4860 Santiago, Chile

ABSTRACT
Dwarf galaxies are ideal laboratories to study the physics of the interstellar medium (ISM). Emission lines have been widely used to this aim. Retrieving the full information encoded in the spectra is therefore essential. This can be efficiently and reliably done using Machine Learning (ML) algorithms. Here, we apply the ML code GAME to MUSE (Multi Unit Spectroscopic Explorer) and PMAS (Potsdam Multi Aperture Spectrophotometer) Integral Field Unit (IFU) observations of two nearby Blue Compact Galaxies (BCGs): Henize 2-10 and IZw18. We derive spatially resolved maps of several key ISM physical properties. We find that both galaxies show a remarkably uniform metallicity distribution. Henize 2-10 is a star forming dominated galaxy, with a Star Formation Rate (SFR) of about 1.2 $M_\odot$ yr^{-1}. Henize 2-10 features dense and dusty (A_V up to 5-7 mag) star forming central sites. We find IZw18 to be very metal-poor ($Z = 1/20\ Z_\odot$). IZw18 has a strong interstellar radiation field, with a large ionization parameter. We also use models of PopIII stars spectral energy distribution as a possible ionizing source for the HeII $\lambda 4686$ emission detected in the IZw18 NW component. We find that PopIII stars could provide a significant contribution to the line intensity. The upper limit to the PopIII star formation is 52% of the total IZw18 SFR.

Key words: galaxies: ISM – abundances – individual: He 2-10 – individual: IZw18 – star formation – evolution

1 INTRODUCTION

Emission lines in the spectra of galaxies contain a huge amount of information on the physical properties of their Interstellar Medium (ISM). The ISM of local Blue Compact Galaxies (BCGs), a sub-class of Dwarf Galaxies, represents a particularly interesting case of study. In fact, since BCGs are low metallicity, compact, star-forming systems, they are thought to represent local analogues of early galaxies (Lequeux et al. 1979; Garland et al. 2015) that will become soon observable in greater detail with forthcoming instruments (e.g., JWST). Given their small distances, local

BCGs can be studied at much higher spatial resolution with respect to high redshift galaxies. Thus, ISM studies of local BCGs can be used as benchmarks for understanding the structure, formation and evolution of high redshift galaxies. The concept of BCG was firstly introduced by Zwicky (1965) to refer to "quasi-stellar galaxies", namely galaxies with pure emission line spectra, initially barely distinguishable from stars (Arp 1965). Since the spectra of BCGs resemble galactic HII regions (Haro 1956; Zwicky 1966; Markarian 1967), these galaxies are also called HII galaxies (Markarian 1967; Sargent & Searle 1970; Melnick et al. 1985; Hazard 1986; Terlevich et al. 1991). This is the case of Henize 2-10 (Corbin et al. 1993), a Wolf-Rayet starburst galaxy with a central radio source, a metallicity of 12+log(O/H) = 8.55 ±

0.02 (Esteban et al. 2014), intense star formation rate (SFR
$\sim 1.9\,\mathrm{M}_\odot\,\mathrm{yr}^{-1}$, see Reines et al. 2011), and the possible pres-
ence of an active massive black hole (Reines et al. 2016, but
see also Cresci et al. 2017).

BCGs have different physical properties com-
pared to other varieties of star-forming galaxies
(Arp1965,Zwicky1966). In fact, their star formation
occurs in short bursts, separated by long ($\sim 10^7$ years)
quiescent periods (Sargent & Searle 1970; Searle & Sargent
1972; Searle et al. 1973; Kunth & Östlin 2000) resulting
in young stellar populations (with commonly accepted
indications of older underlying population, Tolstoy et al.
2009), and a small amount of dust. Very low metallicity
values have been indeed measured in several BCGs: IZw18
(12+log(O/H) = 7.17 ± 0.04, Searle & Sargent 1972; Dufour
et al. 1988; Skillman & Kennicutt 1993); the starburst
galaxy SBS 0335-052W (Izotov et al. 1990, 1997, 2005,
2009) with 12+log(O/H) = 7.13 ± 0.02 (Izotov et al. 2009);
the irregular galaxy DDO 68 (12+log(O/H) = 7.21 ± 0.03,
Pustilnik et al. 2005; Berg et al. 2012); the low-luminosity
dwarf Leo P (12+log(O/H) = 7.17 ± 0.04, McQuinn et al.
2015; Skillman et al. 2013); AGC 198691, the most metal
poor galaxy known in the local Universe (12+log(O/H) =
7.02 ± 0.03, Hirschauer et al. 2016).

Most of the results reported above have been obtained
by adopting diagnostics based on emission-line ratios. An
alternative, promising approach relies on Machine Learning
(ML) techniques (Ucci et al. 2017, 2018, hereafter U17 and
U18). In this work, we study the ISM physical properties
of Henize 2-10 and IZw18 by processing their Integral Field
Unit (IFU) observations with the ML code GAME (GAlaxy
Machine learning for Emission lines U17; U18). The advan-
tage of this code relies on the fact that it is possible to infer
simultaneously several ISM physical properties by using all
the information in the spectra. The purpose of this work is
to apply GAME in the case of two well-studied examples of
local BCGs in view of future applications, especially at high
redshifts.

The paper is organized as follows: in Sec. 2, we summa-
rize the main features of the GAME code; in Sec. 3 and 4, we
present the results for Henize 2-10 and IZw18, respectively;
in Sec. 5 we discuss and summarize the main results of this
study.

2   INFERRING ISM PHYSICAL PROPERTIES

GAME is a ML code that infers the ISM physical properties
by analyzing the emission line intensities in a galaxy spec-
trum (for the complete description see U17; U18). The code
is based on a Supervised ML algorithm, and it is trained with
a library of 100,000 synthetic spectra spanning many differ-
ent ISM phases, including HII (ionized) regions, PDRs and
neutral regions (U17; U18). The library of synthetic spec-
tra is generated by using the photoionization code CLOUDY
v13.03 (Ferland et al. 2013) by varying the total (i.e., HI
+ HII + H_2) gas density (n), total column density (N_H),

ionization parameter[1] (U), and metallicity[2] (Z); the library
contains PopII and PopIII stellar populations (see U18). The
emission line library is then processed in order to account for
noise in the observations (U18). Given a set of input lines in
a spectrum, the ML performs a training on the library, then
evaluates the line intensities to give a determination of the
physical properties; each physical property is determined by
the AdaBoost ML algorithm separately and independently
(U17). The errors on the input emission line intensities and
the uncertainties on the physical properties determinations
have been taken into account and they have been included
in the analysis (U18).

It is important to notice that GAME does not use a pre-
selected subset of emission line ratios (i.e., [NII]/Hα, R_{23}),
but rather reconstructs the ISM properties of galaxies ex-
ploiting all the lines available in the input, including the
faint ones. As showed in U18, the accuracy of the determi-
nation of the physical properties improves with an increasing
number of emission lines.

The physical properties directly inferred by GAME in
this work are: gas density (n), column density (N_H), ioniza-
tion parameter (U), metallicity (Z), Far-Ultraviolet (FUV,
6 - 13.6 eV) flux (G)[3], visual extinction (A_V). Starting from
these properties it is possible to derive information also on
the star formation surface density (Σ_{SFR}), and the gas mass
surface density (Σ_{gas}), as detailed below. We can use N_H
maps to obtain an estimate of the total gas mass contained
in each spaxel of the map:

$$M = \mu m_H N_H A_{spax}, \tag{1}$$

where μ is the mean molecular weight (in the following we
assume $\mu = 1.4$), m_H is the hydrogen atom mass, and A_{spax}
is the spaxel area. The gas mass surface density is then

$$\Sigma_{gas} = \mu m_H N_H. \tag{2}$$

Using these quantities, we can also infer the star
formation rate surface density (Σ_{SFR}), by assuming a
Schmidt-Kennicutt relation (Schmidt 1959; Kennicutt 1998;
Krumholz et al. 2012):

$$\Sigma_{SFR} = \eta \frac{\Sigma_{gas}}{t_{sf}} \tag{3}$$

where η is the star formation efficiency and t_{sf} is the star
formation time scale. As shown by Krumholz et al. (2012),
the relation is well fitted in a variety of environments by
using $t_{sf} = t_{ff}$, where t_{ff} is the gas free-fall time, and $\eta =$

---

[1] In this work we adopted the following definition for the ioniza-
tion parameter: $U = Q(H)/(4\pi R_S^2 nc)$, where $Q(H)$ is the ionizing
photon flux, c is the speed of light and R_S is the Strömgren ra-
dius.
[2] In the library we assumed fixed solar abundance ratios for all
the elements (U18).
[3] For a given library spectrum G, n, and U are directly related,
but they are determined independently by the ML algorithm, as
explained in the text.

0.015. Thus we can write eq. 3 in terms of quantities directly derived from GAME (i.e., n and N_H):

$$\Sigma_{SFR} = 0.015 \, m_H^{3/2} N_H \sqrt{\frac{32Gn}{3\pi}}. \quad (4)$$

Alternatively it is also possible to derive the SFR from the Hα line intensity after correcting for the dust extinction, using specific calibrators (Kennicutt 1998; Calzetti et al. 2007; Kennicutt & Evans 2012). In Sec. 3.1.5 we will show a comparison between the SFR estimated via eq. 4 and the calibration from Calzetti (2008) with different dust extinction laws. We now apply GAME to the study of two BCGs, Henize 2-10 and IZw18.

3 HENIZE 2-10

The blue compact local galaxy Henize 2-10 (hereafter He 2-10) can be considered as a prototype of an HII (Allen et al. 1976) Wolf-Rayet (Dodorico et al. 1983; Kawara et al. 1987; Conti 1991; Vacca & Conti 1992) starburst galaxy. It is located at a distance of 8.23 Mpc (Tully et al. 2013) with a corresponding angular scale of 40 pc/″, and its core has an optical extent less than 1 kpc. He 2-10 has been extensively studied both in the optical and in the infrared wavelength ranges (Vanzi & Rieke 1997; Vacca et al. 2002; Engelbracht et al. 2005), up to the sub-millimeter (Bayet et al. 2004; Johnson et al. 2017). It has a stellar mass of $(10 \pm 3) \times 10^9$ M$_\odot$ (Reines et al. 2011; Nguyen et al. 2014). The estimated SFR is ~ 1.9 M$_\odot$ yr^{-1} (Reines et al. 2011), as revealed by classical indicators such as the Hα (Méndez et al. 1999) and the 24 μm flux (Engelbracht et al. 2005). In Fig. 1, we show the Hα image of He 2-10. The bulk of the Hα emission is located in two central emitting regions (hereafter Region A and B) separated by $\sim 2''$ (~ 80 pc).

An unresolved non-thermal nuclear source has been found in the nucleus of He 2-10 (Kobulnicky & Johnson 1999; Johnson & Kobulnicky 2003). This source (designated as knot #3) is located between Regions A and B in Fig. 1. Reines et al. (2011) linked this source to the presence of a compact X-ray emission detected with Chandra observations (Kobulnicky & Martin 2010). The size of this emitting region has been constrained to be < 1 pc $\times$ 3 pc (Reines & Deller 2012) and recently associated with the presence of a weakly accreting super massive black hole having mass $\log(M/M_\odot) \sim 6.3$ (Reines et al. 2016). The origin of the X-ray emission in He 2-10 is still debated (Cresci et al. 2017). We further discuss this point in Appendix A where we show that on scales larger than ~ 4 pc from the center, the radiation field is dominated by stars.

3.1 ISM physical properties in He 2-10

In this section, we present a systematic overview of the ISM physical properties in He 2-10, inferred by applying GAME (U17; U18) to MUSE (Multi Unit Spectroscopic Explorer, Bacon et al. 2010) optical integral field observations taken from Cresci et al. (2017). We have a total of $321 \times 328 = 105,288$ spaxels with a spatial sampling of $0.2'' \times 0.2''$. The spectral resolution (i.e., $R = \lambda/\Delta\lambda$) goes from 1750 at 4650 Å to 3750 at 9300 Å (Cresci et al. 2015, 2017). The emission
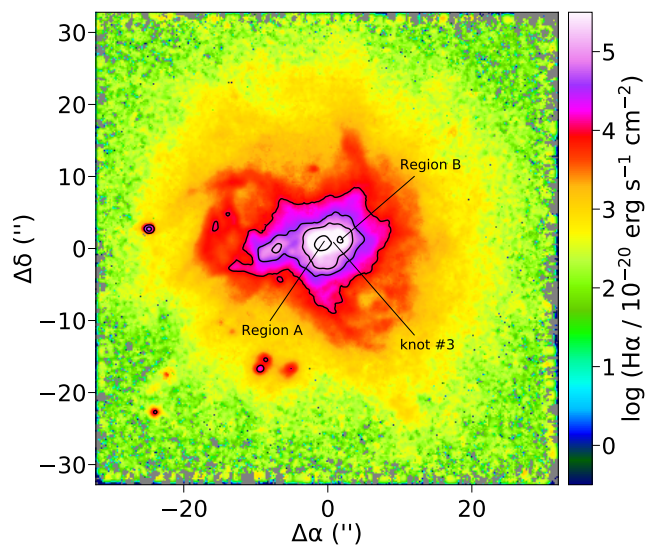
Figure 1. Hα image of Henize 2-10 (Cresci et al. 2017). Black lines show the contours of the Hα emission (80, 10, 4, and 1 in units of 10^{-16} ergs s^{-1} cm^{-2}). The Hα contour levels are the same as in Cresci et al. (2017) in order to be able to directly compare their figures. Shown are the two regions A and B where the Hα flux peaks. We also show the radio source designated by Johnson & Kobulnicky (2003) as knot #3. The field of view of the image is $(64'')^2$ corresponding to a physical size of $(2.56 \text{ kpc})^2$.

Table 1. Emission lines and wavelengths used to analyze the galaxy He 2-10. The third column reports the fraction of spaxels with a detected and fitted line, having SNR > 3.

line	wavelength [Å]	fraction of spaxels
Hβ	4861	20 %
[O III]	5007	15 %
He I	5876	3 %
[O I]	6300	2 %
Hα	6563	36 %
[N II]	6584	18 %
He I	6678	1 %
[S II]	6717	15 %
[S II]	6731	11 %
[S III]	9069	2 %

lines used as input for GAME are reported in Table 1 along with the fraction of spaxels with a detected and fitted line, having SNR > 3. For details on the line fitting procedure we refer the reader to Cresci et al. (2017).

The resulting maps (median radial profiles[4] centered on $(\Delta\alpha,\Delta\delta)=(0,0)$) of the inferred physical properties are reported in Fig. 2 and 5 (Fig. 3 and 6). As observations outside the center of the galaxy become noisy, we selected only the lines with SNR > 3 (see Table 1). Then we analyzed the spaxels with at least 6 lines satisfying this condition (see

---

[4] Because the physical properties distributions in the inferred maps are relatively spread, we preferred to use the median instead of the average in order to prevent an increase of the radial profiles purely driven by the presence of few high values.
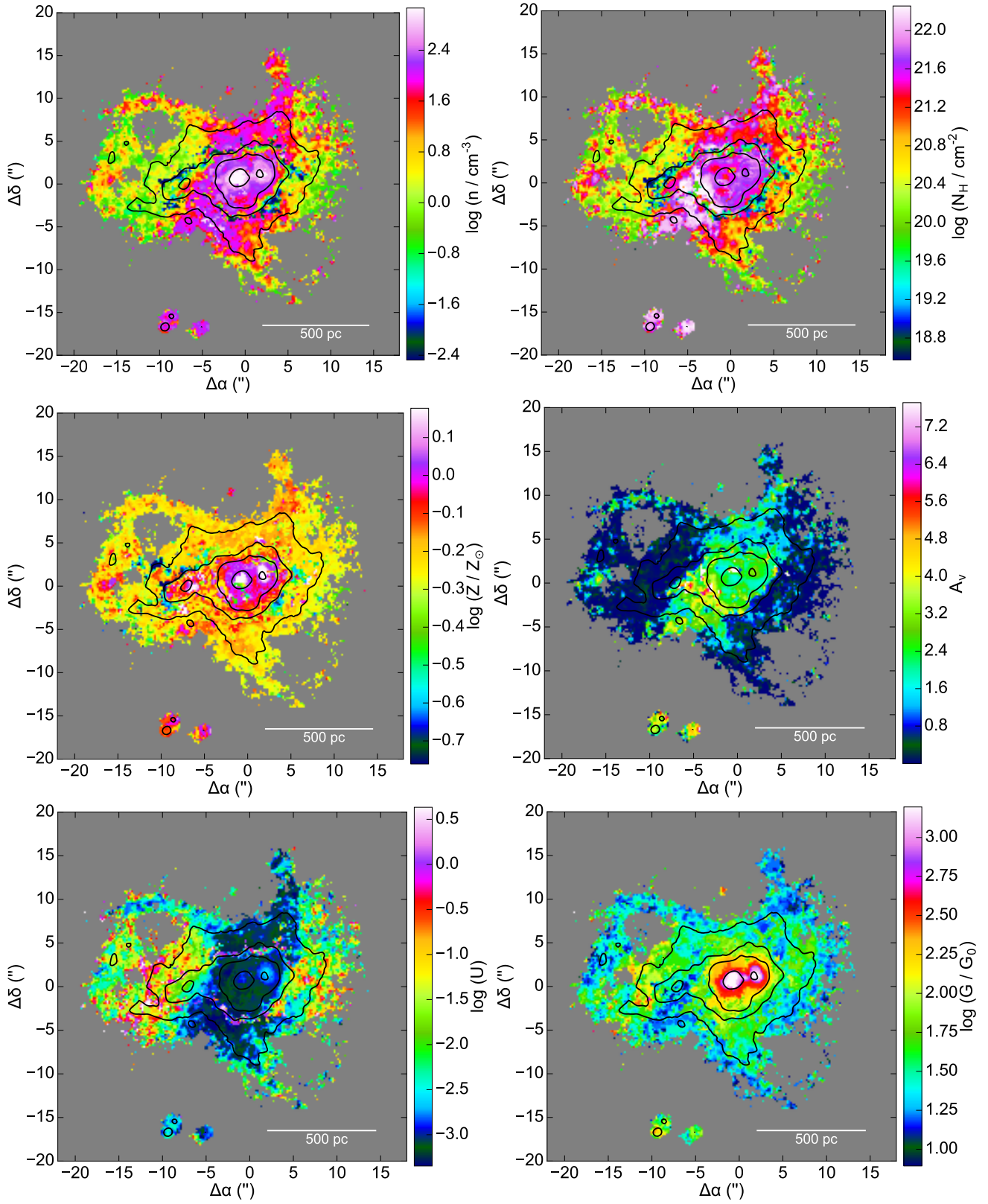
Figure 2. Maps of the ISM physical properties inferred for the local galaxy He 2-10 using the code GAME (Ucci et al. 2017, 2018): density (n), column density (N_H), metallicity (Z), visual extinction (A_V), ionization parameter (U) and the FUV flux in Habing units (G/G_0). As in Fig. 1, black lines show the contours of the Hα emission line (80, 10, 4, and 1 in units of 10^{-16} ergs s^{-1} cm^{-2}).
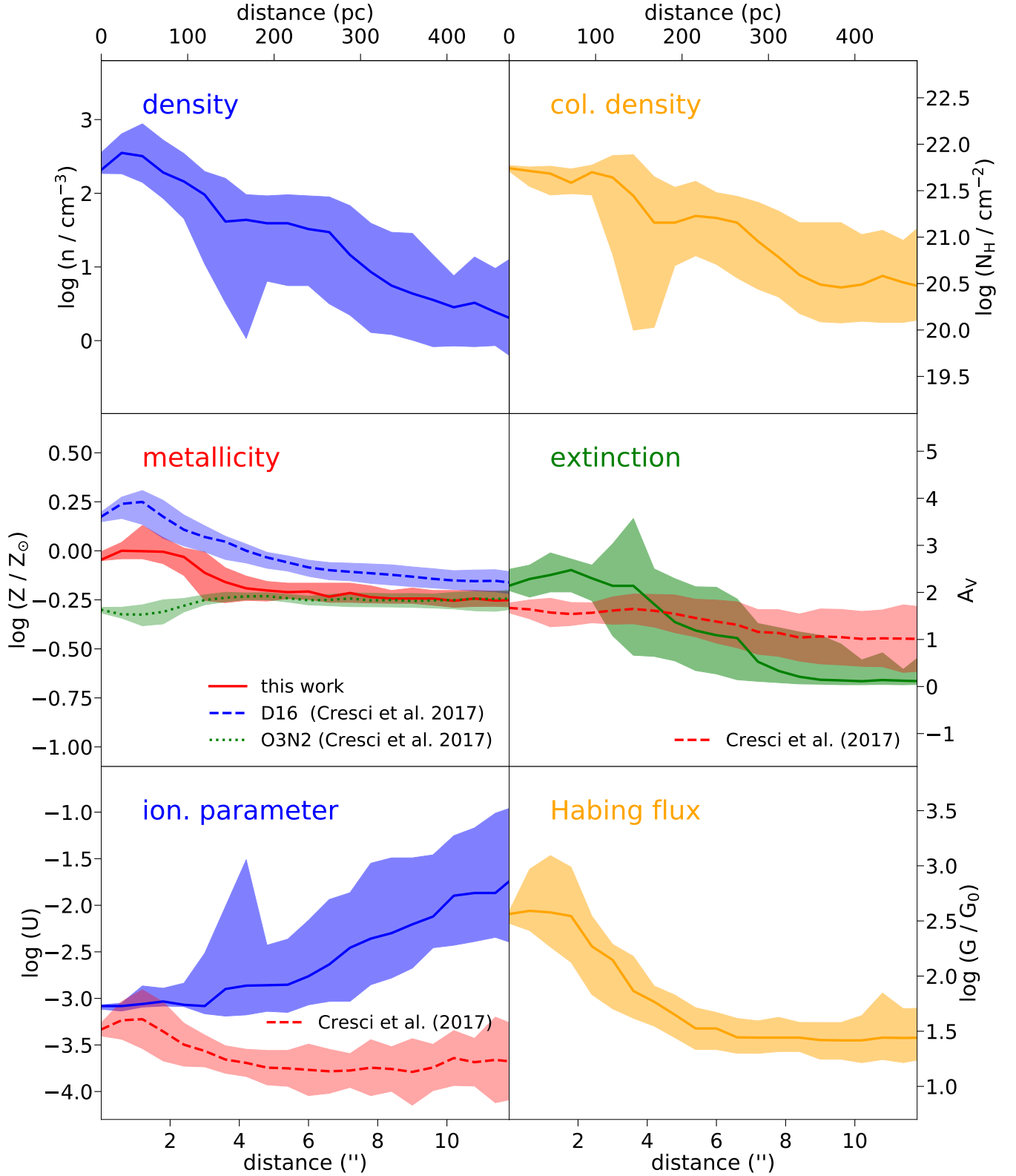
Figure 3. Median radial profiles (median of the inferred physical property values in annular bins of 0.6″) of the He 2-10 ISM physical properties obtained from the maps shown in Fig. 2, centered on $(\Delta\alpha, \Delta\delta)=(0,0)$. Upper and lower shaded regions denote respectively the 2nd and 3rd quartiles. For metallicity, extinction and ionization parameter, we also report the radial profiles as inferred by Cresci et al. (2017).
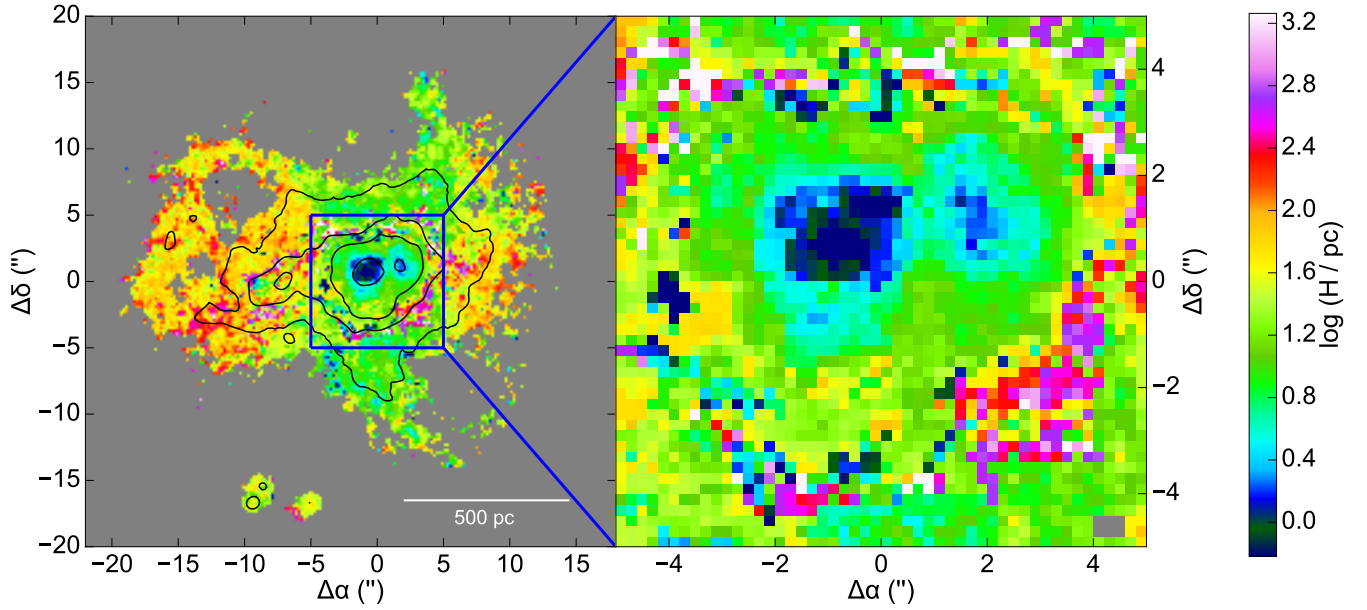
Figure 4. *Left panel*: "effective" scale height defined as $H = N_H/n$. As in Fig. 1, black lines show the contours of the Hα emission line (80, 10, 4, and 1 in units of 10^{-16} ergs s^{-1} cm^{-2}). *Right panel*: zoom on the blue box.
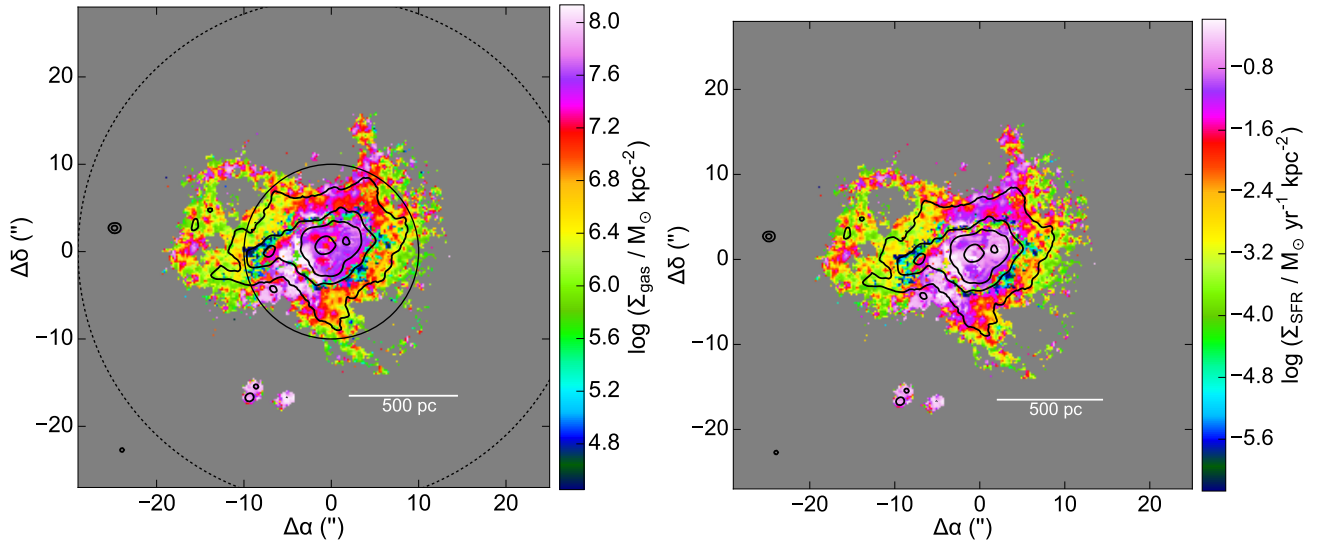

Figure 5. Gas mass surface density (Σ_{gas}, *left panel*) and Star Formation surface density (Σ_{SFR}, *right panel*) for the local galaxy He 2-10. As in Fig. 1, black lines show the contours of the Hα emission line (80, 10, 4, and 1 in units of 10^{-16} ergs s^{-1} cm^{-2}). Inner and outer black circles denote the areas covered by the CO observations of Vanzi et al. (2009) and Kobulnicky et al. (1995), respectively (see text for details).

discussion in Appendix D of U18). These spaxels are the ones plotted in each panel of Fig. 2 and 5. In Appendix B we also report the uncertainties on the physical properties computed with GAME on all the spaxels visualized.

3.1.1 Gas density

The gas density map (n) in the upper left panel of Fig. 2 shows that the highest density is reached close to Regions A and B, where $\log(n/\text{cm}^{-3}) \sim 3.3$. For distances $d \gtrsim 5''(\gtrsim 200 \text{ pc})$ from the center, the median density radial profile

in the galaxy decreases until a distance of ~ 350 pc around a value of $\log(n/\text{cm}^{-3}) \sim 0.5$ (see Fig. 3). The upper right panel of Fig. 2 shows that column densities in the He 2-10 central region (i.e., within $10''$ from the center) vary from $\sim 10^{20}$ cm^{-2} up to $\sim 3 \times 10^{22}$ cm^{-2}, consistently with results found in literature (Baas et al. 1994; Kobulnicky et al. 1995; Meier et al. 2001; Santangelo et al. 2009; Cresci et al. 2017).

The left panel of Fig. 4 shows the map of the the effective scale height of the disk, defined as $H = N_H/n$. In the right panel, we zoom in the central region [$5'' \times 5''$, i.e. 200 $\times$ 200 pc^2], where the uncertainties are smaller (see Fig. B1
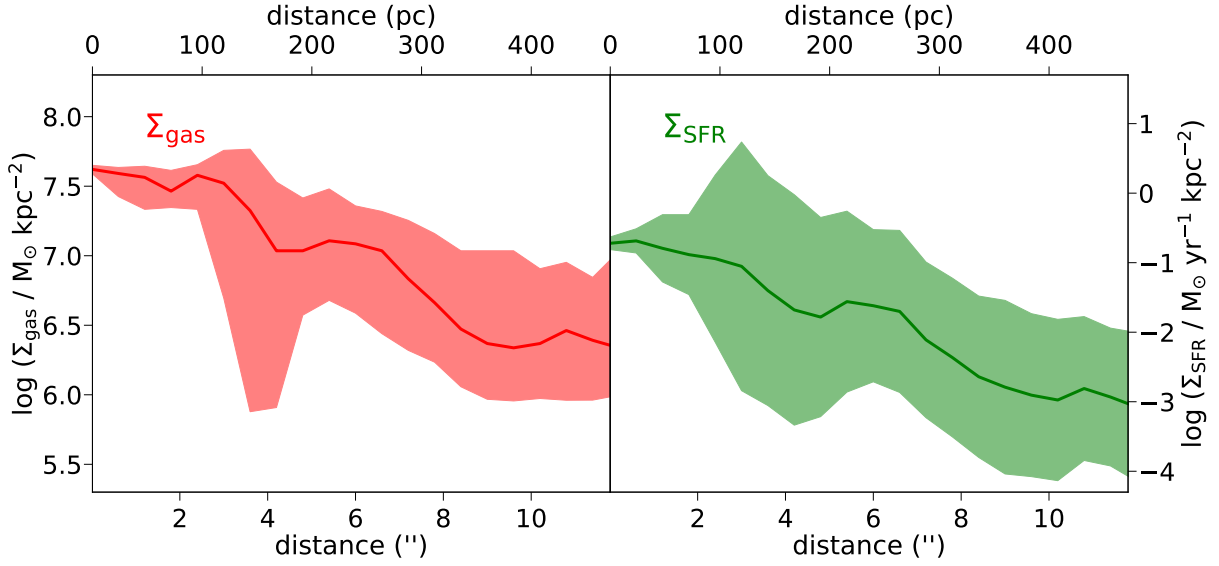
Figure 6. Median radial profiles (median of the inferred physical property values in annular bins of 0.6″) of He 2-10 Σ_{gas} and Σ_{SFR} (*left* and *right panel*, respectively) obtained from the maps shown in Fig. 5, and centered on $(\Delta\alpha,\Delta\delta)=(0,0)$. Upper and lower shaded regions denote respectively the 2nd and 3rd quartiles.

in Appendix B). In the central region, we find a relatively small height of the disk, i.e. $-0.5 \lesssim \log(H/pc) \lesssim 1.5$ $(0.3 \lesssim H/pc \lesssim 30)$. This is the typical dimension of Giant Molecular Clouds (GMCs) that we are resolving in the center of the galaxy. Region A and B, with their high values of densities and metallicities, and given also the high Hα and FUV flux G, can be identified as the sites of intense star formation.

3.1.2 Metallicity

The metallicity map and the corresponding radial profile are reported in the central left panels of Fig. 2 and 3, respectively. We find that Region A and B $(d \lesssim 4'')$ are characterized by super-solar values $(\log(Z/Z_\odot) \sim 0.2 - 0.3)$, while at larger distances $(4'' \lesssim d \lesssim 10'')$ the metallicity is slightly sub-solar (i.e., $\log(Z/Z_\odot) \sim -0.15$) and remarkably uniform (within a factor of ~ 2). The obtained average metallicity $(12+\log(O/H) \sim 8.6)$ is the one expected from the mass-metallicity relation for a galaxy with a stellar mass of M$_* \sim 10^{10}$ M$_\odot$, i.e. $12+\log(O/H) \sim 8.7$ (Sánchez et al. 2017).

We also compare our results with the radial profiles of Cresci et al. (2017) who adopted the D16 (Dopita et al. 2016) and the O3N2 (Curti et al. 2017) calibrators (Fig. 3). The metallicities obtained with GAME are between the results obtained through the O3N2 and D16 calibrators. In particular, in Fig. 7 we compare the distributions of the derived metallicity values inferred through the 3 different methods. The distribution obtained by GAME covers the same values inferred with the O3N2 and D16 methods, but spans a larger range (i.e., $-1.0 \lesssim \log(Z/Z_\odot) \lesssim 0.3$). The standard deviations of the metallicity values inferred with the three approaches are respectively: $\sigma(\text{GAME}) \sim 0.13$, $\sigma(\text{O3N2}) \sim 0.06$, $\sigma(\text{D16}) \sim 0.10$. The difference in the results obtained between this work and Cresci et al. (2017) can be ascribed to the fact that while the O3N2 and D16 diagnostics account for ionized regions only, the GAME results are based on a library spanning several phases of the ISM (U17; U18). In fact, the
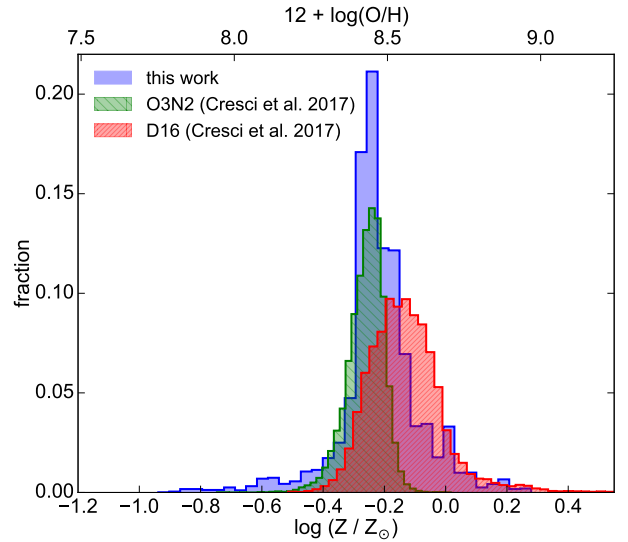

Figure 7. Distributions of the He 2-10 metallicity (central left panel of Fig. 2). The blue shaded histogram reports the inferred values for the metallicity obtained in this work. The green and red shaded regions show the results obtained by Cresci et al. (2017) using the *O3N2* line ratio and the diagnostic by Dopita et al. (2016) (*D16*), respectively.

physical properties are inferred taking into account not only ionized gas constraints (see Table 1), but also lines coming from neutral (i.e., [OI]) and partially neutral regions (i.e., [SII]). In order to test this hypothesis, we have repeated the analysis removing the [OI] and [SII] lines, and we have checked whether the metallicity measurements are affected. In Fig. 8, we report the metallicity inferred with GAME using two different sets of input emission lines: one with all the input lines reported in Table 1 (*left panel*), and one using only purely ionized input lines (*right panel*), i.e. removing the [OI] and [SII] lines. In Fig. 9 we show the median radial

profiles of the maps reported in Fig. 8, compared with the previous estimates by Cresci et al. (2017). It is evident that the metallicity values inferred from ionized lines only (especially in the central region, $d \lesssim 5''$), are lower than the ones obtained using the full set of input emission lines (i.e., the one that contains also neutral and partially neutral emission lines).

3.1.3 Dust extinction

In Fig. 2, we show the map of the visual extinction A_V. In the central region of the galaxy (i.e., $d \lesssim 5''$) A_V ranges between 1 and 5 magnitudes while in the outer regions (i.e., $d \gtrsim 8''$), the A_V median radial profile flattens to ~ 0.1 mag (see Fig. 3), although with a large dispersion.

Vacca & Conti (1992) measured $E(B - V) = 0.54$ (corresponding to $A_V = 1.7$ mag, assuming $R_V = 3.1$) from the Balmer decrement in optical slit spectroscopy. Cresci et al. (2017) obtained from optical lines $A_V \sim 2.3$ in Region B. Cabanac et al. (2005) found $A_V = 1.25$ ($A_V = 10.5$) over an aperture of $2.4'' \times 15.6''$ centered on the nucleus from the $H\alpha/Br\gamma$ ($Br\gamma/Br10$) ratio (see also Kawara et al. 1989). From the $Br12/Br\gamma$ ratio Cresci et al. (2010) obtained $A_V = 1.5$ - 12 mag in a region within $2 - 3''$ from the center. The inferred extinction found in literature from IR observations is higher with respect to the A_V estimated from the optical wavelength range. Since the central region of He 2-10 is a complex system characterized by the presence of absorbing material (i.e., gas and dust) mixed with emitting sources (Martín-Hernández et al. 2006), classic diagnostics based on optical lines do not allow A_V measurements into dust-embedded star forming regions, as IR data do.

Fig. 2 shows that A_V mildly correlates with n, as quantified in Fig. 13 with a correlation coefficient $C = 0.64$. In the star-forming Regions A and B, we obtain $A_V \gtrsim 2 - 3$ mag. The visual extinction reaches a peak in the SW part centered at $(\Delta\alpha, \Delta\delta) = (-4,-3)$, at $d \sim 4''$ from the center, where there is a region highly correlated with high column densities ($N_H \gtrsim 10^{22}$ cm^{-2}). It is a region with $\Sigma_{gas} > 10^8$ M$_\odot$ kpc^{-2} and where most of the gas mass is located (e.g., Fig. 5), and already associated in Cresci et al. (2017) with an accreting cloud detected in CO observations.

3.1.4 Interstellar radiation field

We characterize the radiation field of He 2-10 in terms of the FUV flux G and the ionization parameter U, whose maps are shown in the bottom right and left panel of Fig 2, respectively. From the median radial profile, the FUV flux in Habing units[5] is $G/G_0 \sim 10^3$ in the center of the galaxy (in correspondence of the highly star forming regions A and B), while at larger distances (i.e., $d \gtrsim 4''$) it flattens around $G/G_0 \sim 10^{1.5}$. For what concerns the ionization parameter, $U \sim 10^{-3}$ in the central regions ($d \lesssim 4''$), while at larger distances $U \sim 10^{-1.5}$. Our results are consistent with the ones reported by Cresci et al. (2017) in the inner region of the galaxy while, at $d \gtrsim 2''$, GAME infers U values up to two

---

orders of magnitude larger[6]. In what follows, we analyze the physical origin of our findings.

The U profile depends on G and n according to the following relation[7]: $G/G_0 \sim 10^3 Un$. In Fig. 10, we compare the radial median profile of U (blue line/shaded region) with the one of $10^{-3} G/G_0 \, n^{-1}$ (red line/shaded region), where U, G, and n are the values inferred by GAME independently. This figure shows that the expected physical trend is correctly recovered by the ML algorithm. At small distances ($d < 4''$), large values of the FUV flux $G/G_0 \sim 10^3$ are compensated by much larger values of the gas density ($n \sim 10^3$ cm^{-3}), thus providing a small value of U ($\sim 10^{-3}$). Vice versa, at larger distances, the strong decrease of the gas density ($\log(n/\text{cm}^{-3}) \sim 0$, because of the strong anti-correlation with U, see Fig. 13) and the flattening of the FUV flux at the value $G/G_0 \sim 10^{1.5}$, combine into a large U value ($\gtrsim 10^{-2}$).

Cresci et al. (2017) used the line ratio [SIII]/[SII] to derive U, using the calibrations of Kewley & Dopita (2002). Our results are consistent with their findings only within few arcsec ($\sim 2"$) from the center of the galaxy, while our U values are larger in the outer regions. However, note that the U determination has large typical uncertainties. Thus, the U determination cannot be considered reliable in the outer region. The poor determination of U with respect to the other variables from GAME has been already discussed in U17. However, the discrepancy between our findings and the results from Cresci et al. (2017) (see Fig. 3), following what we demonstrated in Sec. 3.1.2, could be ascribed to the fact that we used the full set of input emission lines available with no assumptions about the underlying emitting phase (i.e., without assuming emitting HII regions only). As evident from Fig. 12 (see also Fig. 11), the difference between the radial profiles assuming only ionized lines, reduces to ~ 0.5 dex (i.e, a factor of three). If we assume instead the full set of available lines, at large radii ($d \gtrsim 9''$), the difference is $\gtrsim 1$ dex.

3.1.5 Gas mass and SFR surface density

We computed the gas mass surface density Σ_{gas} (see eq. 2) by considering the spaxel area $A_{spax} = 64$ pc^2.

Kobulnicky et al. (1995) estimated a molecular (atomic) hydrogen mass of $1.6 \pm 0.1 \times 10^8$ ($1.9 \pm 0.1 \times 10^8$) M$_\odot$ from CO(1-0) and CO(2-1) detections. More recent observations based on CO(3-2) emission (Vanzi et al. 2009) provide a molecular mass of 1.4×10^7 M$_\odot$. In Fig. 5, the solid and dashed lines correspond to the sizes of the regions covered by the CO observations of Kobulnicky et al. (1995) (a radius of $\sim 23''$) and Vanzi et al. (2009) (a radius of $\sim 10''$),
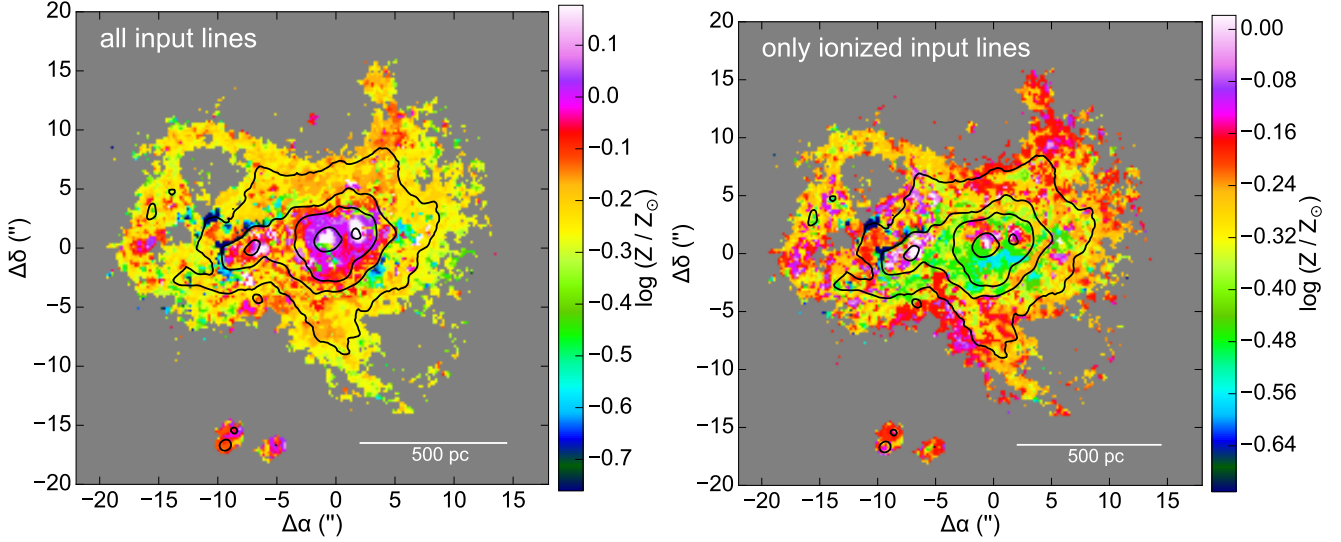

Figure 8. *Left panel:* map of the ISM metallicity (Z) inferred for He 2-10 using all the input lines reported in Table 1. *Right panel:* map of Z inferred for He 2-10 using only the ionized input lines reported in Table 1 (i.e., excluding the [OI] and [SII] lines). As in Fig. 1, black lines show the contours of the Hα emission line (80, 10, 4, and 1 in units of 10^{-16} ergs s^{-1} cm^{-2}).
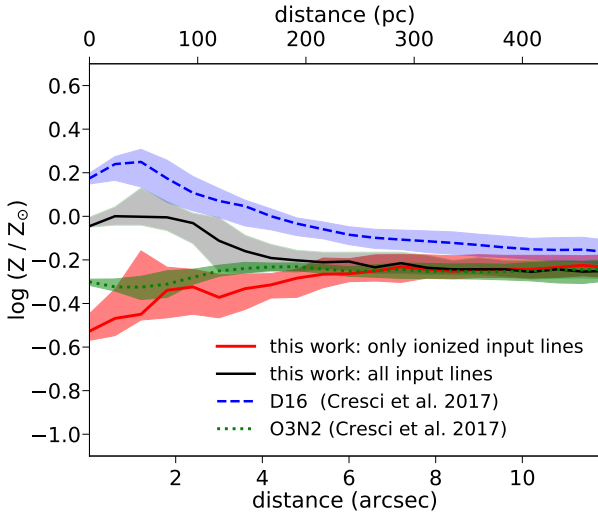

Figure 9. Median radial profiles (median of the inferred physical property values in annular bins of 0.6″) of the He 2-10 metallicity (Z) obtained from the maps shown in Fig. 8, centered on $(\Delta\alpha, \Delta\delta)=(0,0)$. Upper and lower shaded regions denote respectively the 2nd and 3rd quartiles. We also report the radial profiles as inferred by Cresci et al. (2017).

Figure 10. Median radial profile of the He 2-10 ratio between the scaled FUV flux and the density obtained from the maps shown in Fig. 2 (see text for details). Upper and lower shaded regions denote respectively the 2nd and 3rd quartiles. For comparison purposes, we also show the radial profile for the ionization parameter U that follows the same trend.

respectively. By summing up the contribution from spaxels within the outer and inner regions, we obtain a total gas mass of 1.4×10^8 M$_\odot$ and 1.9×10^7 M$_\odot$, respectively, in good agreement with previous estimates.

For what concerns the SFR, we adopt two different approaches. Firstly, by using eq. 4, we compute the SFR surface density shown in the right panel of Fig. 5. By summing up the contribution from all spaxels we obtained SFR = 1.2 M$_\odot$ yr^{-1}. Secondly, we infer the SFR from the Hα map and we correct it for the attenuation through the Calzetti law. For a stellar population with constant SFR over the past 100 Myr, forming stars with an IMF consisting of two power
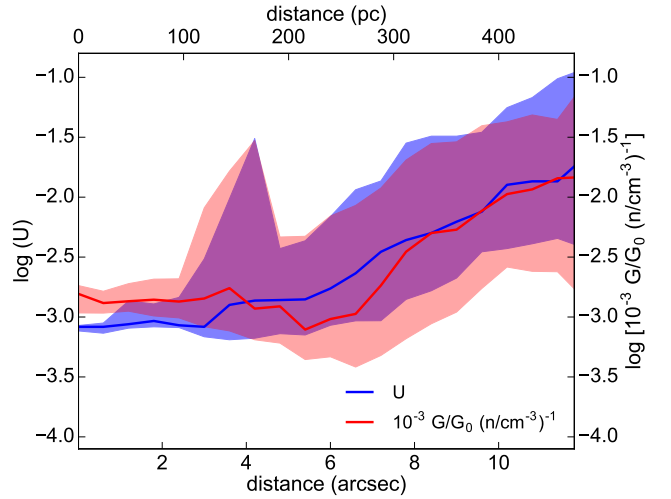
laws (slope -1.3 in the range 0.1 - 0.5 M$_\odot$ and slope -2.3 in the range 0.5 - 120 M$_\odot$), Calzetti (2008) reports:

$$\mathrm{SFR(M_\odot yr^{-1})} = 5.3 \times 10^{-42} \mathrm{L(H\alpha)(erg/s)}, \qquad (5)$$

where L(Hα) is the intrinsic luminosity corrected for absorption and interstellar dust attenuation[8]. Given the fluxes for the Hα line and the map of the extinction A_V (see Fig. 2), the un-corrected SFR is ~ 0.05 M$_\odot$ yr^{-1}. We then corrected the

---

[8] Variations of SFR $\pm20\%$ for younger/older ages and different metallicities are also possible.
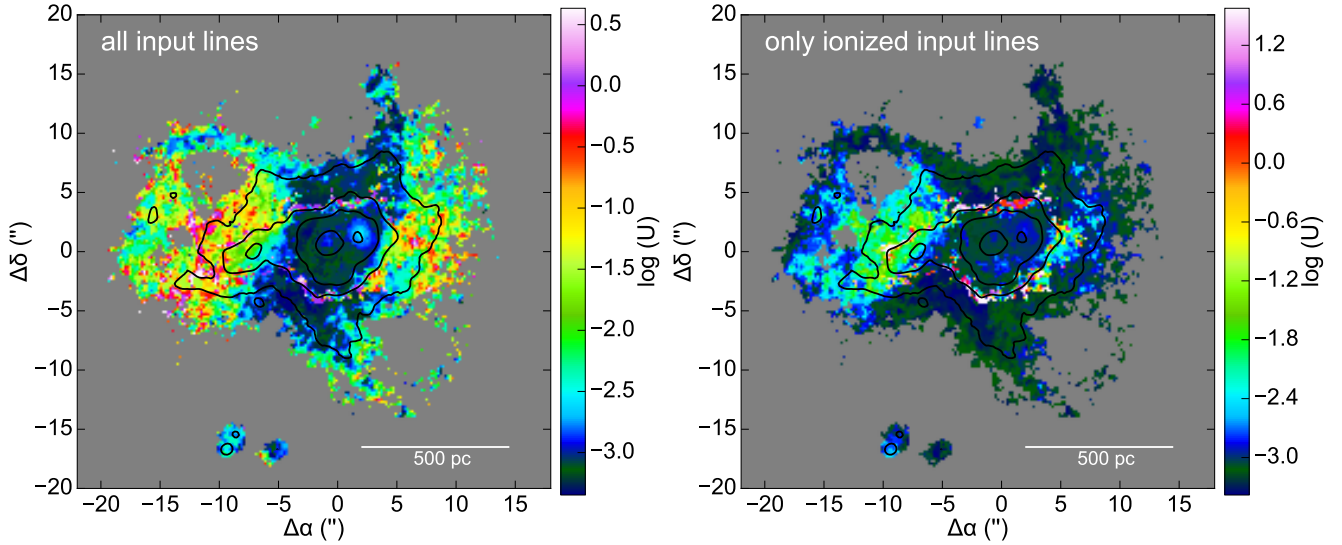
Figure 11. *Left panel:* map of the ISM ionization parameter (U) inferred for He 2-10 using all the input lines reported in Table 1. *Right panel:* map of U inferred for He 2-10 using only the ionized input lines reported in Table 1 (i.e., excluding the [OI] and [SII] lines). As in Fig. 1, black lines show the contours of the Hα emission line (80, 10, 4, and 1 in units of 10^{-16} ergs s^{-1} cm^{-2}).
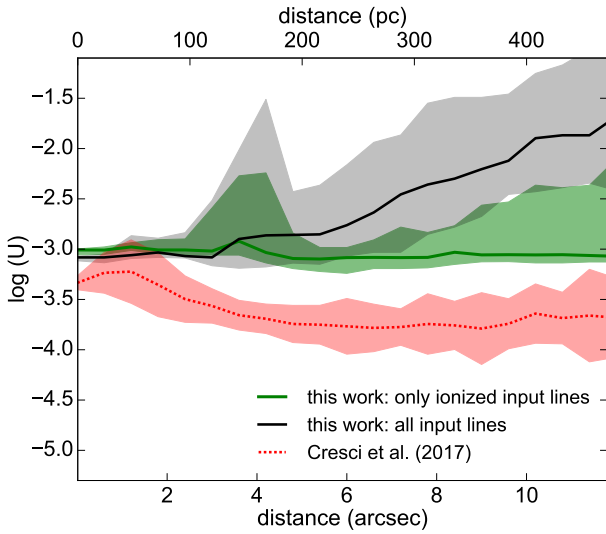

Figure 12. Median radial profiles (median of the inferred physical property values in annular bins of 0.6″) of the He 2-10 ionization parameter (U) obtained from the maps shown in Fig. 11, centered on $(\Delta\alpha,\Delta\delta)=(0,0)$. Upper and lower shaded regions denote respectively the 2nd and 3rd quartiles. We also report the radial profiles as inferred by Cresci et al. (2017).
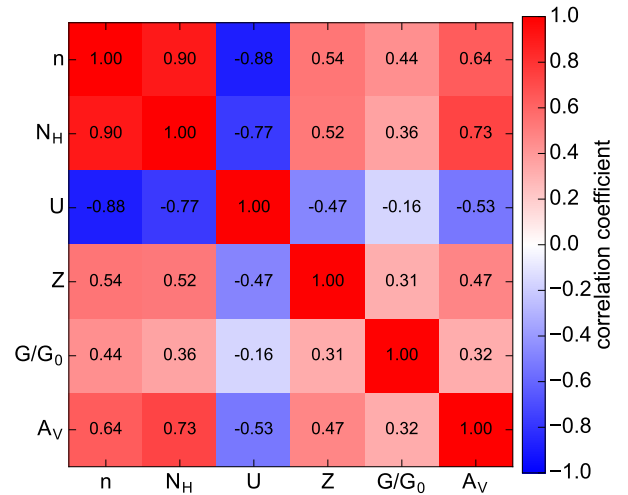

Figure 13. Pearson Correlation coefficient C between the value inferred for the physical properties reported in Fig. 2 for He 2-10. There is strong correlation (anti-correlation) for $0.5 < C < 1.0$ ($-1.0 < CC < -0.5$).

1.26 M$_\odot$ yr^{-1}. This result underlines the strong dependence of the inferred SFR on the assumed extinction curve.

3.2 Physical correlations

We report in Fig. 13 the Pearson correlation coefficients C between the various physical properties inferred by GAME. Given that the spatial resolution of emission line fluxes is limited by the seeing ($\sim 0.68''$, Cresci et al. 2017), in order to have correlation coefficients determinations from independent spaxels, C are computed from 4×4 re-binned maps for the physical properties.

Although determined independently, we find a clear correlation ($C \sim 0.90$) between the density (n) and the column density (N_H). Moreover, the ionization parameter (U) anti-

Hα fluxes using the Cardelli et al. (1989) extinction curve (assuming $R_V = 3.1$). By using eq. 5 with corrected Hα luminosities, and summing up the contribution from the spaxels, we obtained a SFR of ~ 1.44 M$_\odot$ yr^{-1}. This estimate is consistent with the one by Reines et al. (2011) that, by using the Hα (Méndez et al. 1999) and 24 μm (Engelbracht et al. 2005) fluxes, corrected for the Calzetti (Calzetti et al. 2007) attenuation, found 1.9 M$_\odot$ yr^{-1}. By using the SMC (Prevot et al. 1984; Bouchet et al. 1985; Gordon et al. 2003) extinction curve, we can provide another estimate of the SFR. With the same approach described before, by using our extinction map to correct the Hα flux, we obtain: SFR$_{SMC} \sim$

Figure 14. Hα image of the galaxy IZw18 (Kehrig et al. 2016) with a scale of 88 pc/″.

Table 2. Emission lines and wavelengths used to analyze the galaxy IZw18. The third column reports the fraction of spaxels with a detected and fitted line (no SNR cuts applied).

line	wavelength [Å]	fraction of spaxels
[O III]	3727	29 %
[O III]	4363	17 %
Hβ	4861	95 %
[O III]	5007	98 %
[O I]	6300	6 %
Hα	6563	99 %
[N II]	6584	13 %
[S II]	6717	25 %
[S II]	6731	22 %

correlates both with the density ($C \sim$ -0.88) and the column density ($C \sim$ -0.77), due to the dependence of U on the inverse of n. Another expected correlation, such as the one between A_V and N_H is recovered, and we also find $C \sim 0.90$ between A_V and the product $N_H Z$ (see Appendix C).

4 IZW18

Since its discovery (Zwicky 1966), the HII galaxy I Zwicky 18 (hereafter IZw18, also known as Mrk 116), is one of the most intriguing blue dwarf galaxies in the local Universe. Zwicky (1966) described it as a system made by two compact galaxies, recognized now as two compact star forming regions associated with HII regions usually indicated as the NW and SE components (Davidson et al. 1989). It is located at a distance of 18.2 Mpc (Aloisi et al. 2007) with a corresponding angular scale of 88 pc/″. It is considered an analogue of high-redshift galaxies (Lebouteiller et al. 2013, and references therein) and after the first studies (Sargent & Searle 1970; Searle & Sargent 1972; Searle et al. 1973), it continues to keep attraction thanks to its extremely low metallicity: $Z/Z_\odot \sim 0.026$ (Kunth & Sargent 1986; Pagel et al. 1992; Vílchez & Iglesias-Páramo 1998; Izotov & Thuan 1999; Izotov et al. 1999; Lebouteiller et al. 2013; Kehrig et al. 2016). Since the metallicity is homogeneously distributed (Kehrig et al. 2016), IZw18 should host an underlying old population of intermediate/low-mass stars distributed over the whole area of the galaxy (Vílchez & Iglesias-Páramo 1998), although older/fainter ones are more easily detectable only at the system's periphery (Contreras Ramos et al. 2011).

4.1 ISM physical properties in IZw18

In this section, we present the ISM physical properties in IZw18 inferred by applying GAME to IFU data taken from Kehrig et al. (2016). IZw18 data were collected by the Potsdam Multi-Aperture Spectrophotometer (PMAS; Roth et al.

2005, 2010) on the 3.5 m telescope at the Calar Alto Observatory. For more details about the observations and the data reduction we refer the reader to Kehrig et al. (2013, 2015, 2016). For IZw18 we have a total of $16 \times 16 = 256$ spectra. By using the input emission lines reported in Table 2, we obtained the maps of the physical properties shown in Fig. 15 and 16. A_V, Σ_{SFR} and Σ_{gas} are computed as in Sec. 3.1.3 and 3.1.5, respectively. In the case of IZw18, given the lower number of spaxels available with respect to Henize 2-10, we did not apply cuts on SNR in our analysis.

The average uncertainties on the physical properties reported in Fig. 15 are $\sigma(x)/x \sim 0.4 - 0.6$, where x is the physical property expressed in logarithm. As in the case of He 2-10, we find that the metallicity is the inferred physical property with the lowest uncertainties ($\sigma[log(Z)] \lesssim 0.1$, corresponding to a relative uncertainty $\sigma(Z)/Z \lesssim 0.3$).

4.1.1 Gas density

In almost all spaxels we infer density values $\lesssim 10^2$ cm^{-3} (see also Kehrig et al. 2016). The average density is $n \sim 10^{0.7}$ cm^{-3}. For the column density, we infer an average value of $N_H \sim 10^{21}$ cm^2, in agreement with van Zee et al. (1998) that report a gas column density exceeding 10^{21} cm^{-2} mainly located in the SE and NW active star forming regions of IZw18.

4.1.2 Metallicity

In Fig. 15 and 17 we show the map and the metallicity distribution, respectively. No significant metallicity gradient is present: the maximum variation among individual spaxels is in fact within a factor of ~ 3. Although the number of available spaxels is too small for an accurate analysis, this suggests a uniform distribution over spatial scales of hundreds of parsecs (Kehrig et al. 2016). The error-weighted mean metallicity of all spaxels inferred with GAME is $log(Z/Z_\odot) =$ -1.32 ± 0.01, corresponding to 12+log(O/H) = 7.37 ± 0.01 ($\sim 1/20$ solar)[9]. This result is a factor of two larger than the estimate of Kehrig et al. (2016) who found, directly with the

---

[9] Solar gas-phase metallicity is taken to be 12+log(O/H) = 8.69 (Allende Prieto et al. 2001; Asplund et al. 2004), i.e. we assumed the following relation: $log(Z/Z_\odot)$ = 12+log(O/H) - 8.69.
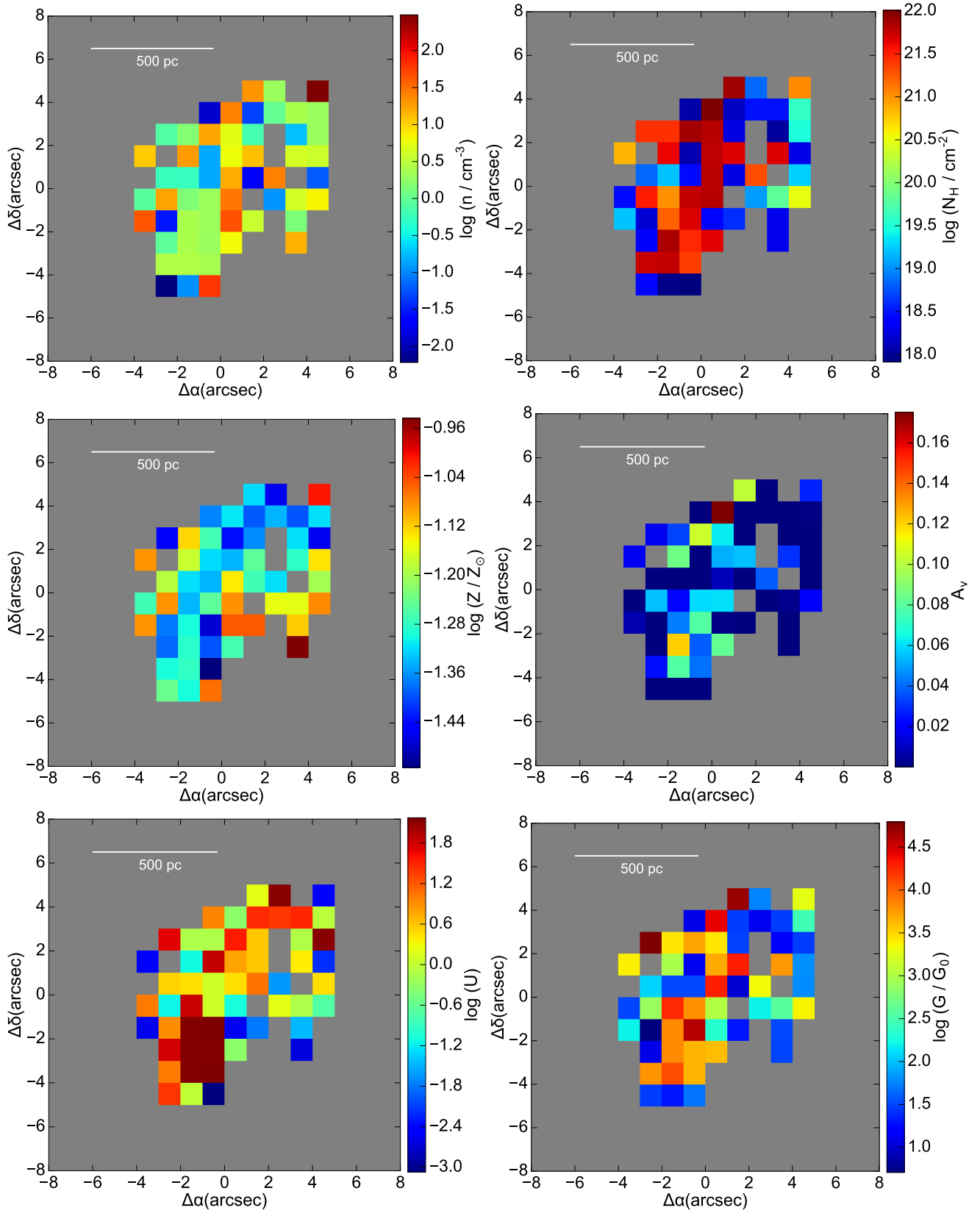
Figure 15. Maps of the ISM physical properties inferred for the galaxy IZw18 using the code GAME (Ucci et al. 2017, 2018): density (n), column density (N_H), metallicity (Z), visual extinction (A_V), ionization parameter (U) and the FUV flux in Habing units (G/G_0).
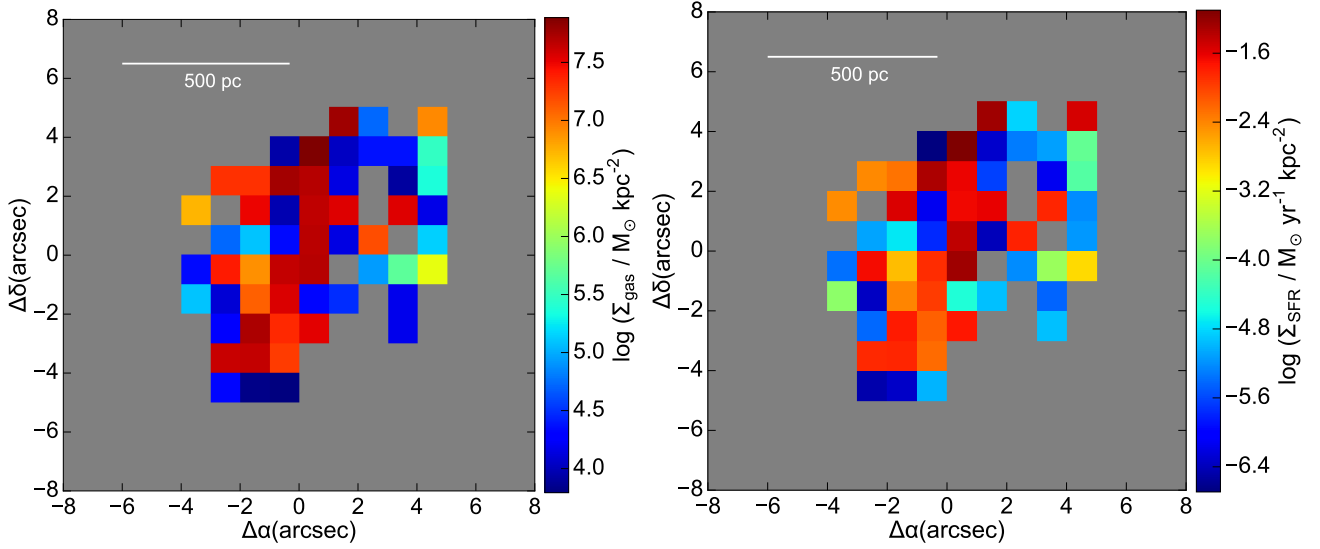
Figure 16. Gas mass surface density (Σ_{gas}, *left panel*) and Star Formation surface density (Σ_{SFR}, *right panel*) for the galaxy IZw18.
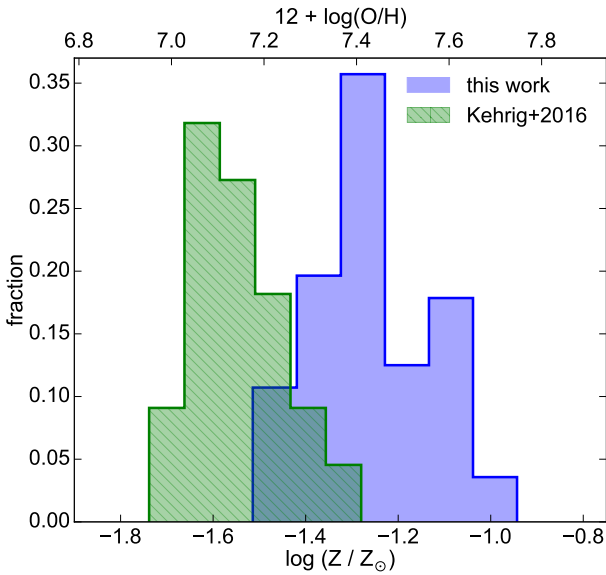

Figure 17. Distribution of metallicity for the spaxels reported in the central left panel of Fig. 15. The blue and green shaded histograms report the results obtained in this work and in Kehrig et al. (2016), respectively.

electron temperature, $12+\log(\text{O/H}) = 7.11 \pm 0.01$ ($\sim 1/40$ solar) (see Fig. 17). This mismatch could be due to the discrepancies between different methods (up to ~ 0.15 dex, see Kewley & Ellison 2008) or to the well known difference up to $0.4 \div 0.5$ dex between direct methods and techniques based on photoionization models (Stasińska 2002; Kennicutt et al. 2003; Garnett et al. 2004; Kewley & Ellison 2008).

4.1.3 Dust extinction

The map of the visual extinction A_V is reported in Fig. 15. We obtain very low values for the visual extinction ($A_V \lesssim 0.20$) with $A_V \sim 0.01$ mag for the majority of the spaxels.

4.1.4 Interstellar radiation field

Regions with higher ionization parameter are preferentially located in the SE knot where we obtained values as high as $U \sim 10^2$. In the rest of the galaxy we found $\log(U) \sim 0.5$ - 1. The most extreme values for U in local analogs of high redshift galaxies can approach unity (e.g., Bian et al. 2016, 2017, 2018). In fact, assuming the relation $L(\text{H}\alpha/\text{erg s}^{-1}) = 1.37 \times 10^{-12}\, Q(H)$ (Osterbrock & Ferland 2006), where $Q(H)$ is the ionizing photon rate in units of s^{-1}, and using the usual definition for U (see footnote 1), we obtain in the SW region $\log(U) \sim -0.5$ - 0.3 (assuming R_S to be 88 pc). However, the GAME output physical property most affected by large uncertainties is the ionization parameter, due to the poorer accuracy in its determination with optical lines only as input (see also U17; U18). A better constraint of U requires a larger number of emission lines (e.g., Fig. D5 in U18), spanning additional wavelength ranges (i.e., UV+optical+IR). Therefore, the extremely high values of U, together with the high G we found could be considered as an additional qualitative indication of the high underlying ionizing flux in this galaxy.

The spatial distribution of G is more uniform across the galaxy, although it is possible to associate higher fluxes in the SE region where $\log(G/G_0) \gtrsim 3.5$. The prominent ionizing flux in the SE knot in our maps, denotes the presence of a clumpy HII component, consisting of numerous knots containing blue stars (Dufour et al. 1996). Such high ionizing fluxes may be originated from the hard SED found in the NW knot, coming from the presence of PopIII stars. (see Sec. 4.2).

4.1.5 Gas mass and SFR surface density

Using the same approach as in Sec. 3.1.5, we obtain Σ_{gas} and Σ_{SFR} in Fig. 16. Given the lack of reliable determinations of N_H and n in some spaxels (i.e., grey areas in Fig. 15 and 16), we can only infer lower limits, SFR $\gtrsim 0.007$ $\text{M}_\odot$ yr^{-1}, and for the total gas mass $\text{M}_{gas} \gtrsim 6.9 \times 10^6$ $\text{M}_\odot$. A previous estimate of $SFR = 0.1$ $\text{M}_\odot$ yr^{-1} was obtained

by Hunt et al. (2005), while Aloisi et al. (1999) provides $SFR = 6 \times 10^{-2}$ M$_\odot$ yr^{-1}. Legrand (2000) and Legrand et al. (2000), by using a spectrophotometric and chemical model, showed that the photometric properties of IZw18 can be reproduced assuming a continuous SFR as low as 10^{-4} M$_\odot$ yr^{-1} lasting for a Hubble time, with a recent burst of star formation superimposed. Recchi et al. (2004) report a SFR of 4-6 $\times 10^{-3}$ M$_\odot$ yr^{-1}. These SFR values are required to generate the blue color of IZw18 (van Zee et al. 1998; Fisher et al. 2014) and the high G and U we found. Galactic winds, produced by stellar winds and SNe could be able to create an outflow and eject part of the ISM. In fact, for such a small galaxy, a SFR of 0.02 M$_\odot$ yr^{-1} can already accelerate the gas and produce the UBV colors, and most of the ionizing luminosity in IZw18 (Martin 1996). The starburst inside this galaxy could also trigger a galactic outflow, with the metals leaving the galaxy far more easily than the unprocessed gas (Mac Low & Ferrara 1999).

4.2 A PopIII-like SED in IZw18 NW?

IZw18 is characterized by an extended nebular HeII $\lambda4686$ emission in its NW component (Kehrig et al. 2015). This implies the presence of a hard ionizing field (i.e., photon energies ≥ 54.4 eV) in this region. This field has been ascribed in the literature (Kehrig et al. 2015, 2016) to the presence of stars with a spectral energy distribution typical of PopIII models (Schaerer 2002; Raiter et al. 2010). In fact, it has been shown (Kehrig et al. 2015) that the HeII-ionizing energy budget cannot be explained by conventional excitation sources (i.e., WRs, shocks, X-ray binaries). Vice versa, one of the possible explanations for this emission is the presence of peculiar very hot, ionizing stars which may be (nearly) metal-free (Kehrig et al. 2015, 2016). To further investigate the origin of the HeII $\lambda4686$ emission, we adopt a modified version of GAME that also predicts the intensity of HeII $\lambda4686$ emission line.

In the left panel of Fig. 18, we report the predicted HeII $\lambda4686$ emission line intensities by considering a reduced library containing only PopII stars (analogous to the ones included in U17). In the central panel is shown the HeII $\lambda4686$ line intensity, obtained by including also PopIII stars (U18). With purely PopII stellar models, it is not possible to obtain emission line intensities compatible with observations (e.g., Fig. 2 of Kehrig et al. 2015): the inferred values are more than one order of magnitude smaller than the observed ones. Adding in the library the contribution from PopIII stars, the HeII $\lambda4686$ intensities can reach values $\gtrsim 10^{-16.0}$ erg s^{-1} cm^{-2}, in agreement with observations in the NW region of IZw18. In Fig. 18 we also show the ratio between the PopII and the (PopII+PopIII) contribution to the HeII $\lambda4686$ intensities. We found that there is a negligible contribution from PopII stars in the NW region, where the ratio is $\ll 1$, denoting the possible evidence of a PopIII population. Although there is X-ray emission dominated by a single point source located in the NW region with no significant contribution of faint diffuse emission, the HeII emission is essentially due to hot stars (Péquignot 2008; Lebouteiller et al. 2017). Our result suggests that PopII stellar populations can not account for the observed HeII$\lambda4686$ flux, while PopIII stars, may provide a substantial contribution to the HeII emission.

We exploit this result to provide an estimate of the PopII/PopIII relative contribution to the total SFR of IZw18. First, we select the spaxel reported in the right panel of Fig. 18 for which the ratio is approximately 1. Given that in these spaxels no PopIII stars contribution is required to explain the HeII emission, we attributed their SFR to PopII stars only. Summing up their contribution, we obtain a value of SFR$_{PopII} \sim 0.0031$ M$_\odot$ yr^{-1}. In the remaining spaxels, where the ratio is $\gtrsim 1$, the SFR resulting from the combination of PopII and PopIII bursts is ~ 0.0039 M$_\odot$ yr^{-1}. We conclude that PopIII stars could explain at most 52% of the total IZw18 SFR (SFR$_{PopIII} \lesssim 0.007$ M$_\odot$ yr^{-1}, see Sec. 4.1.5).

5 CONCLUSIONS

We presented a comprehensive investigation of the ISM physical properties in two Blue Compact Galaxies (BCGs): the starburst galaxy Henize 2-10, and the metal-poor dwarf IZw18. This study was possible taking advantage of a Machine Learning (ML) code called GAME (GAlaxy Machine learning for Emission lines, see U17; U18), specifically designed to infer the physical properties of multi-phase ISM. We applied GAME to MUSE and PMAS IFU observations, obtaining the resolved structure of gas density (n), column density (N_H), ionization parameter (U), metallicity (Z), FUV flux (G), visual extinction (A_V), gas mass surface density (Σ_{gas}), SFR surface density (Σ_{SFR}).

GAME proved to be extremely reliable: although each physical property is treated separately and independently (i.e., a different ML model is constructed for each of the physical properties, see U18), the overall morphology of the inferred maps agree with one each other and the expected correlations between physical properties such as n with N_H (see Fig. 13) hold (see also Appendix C).

Our main conclusions for the galaxy Henize 2-10 can be summarized as follows:

• It is a star-forming dominated galaxy with $SFR \gtrsim 1.2$ M$_\odot$ yr^{-1}, and a total gas mass of $M_{gas} \sim 1.9 \times 10^7$ M$_\odot$.

• The ionization parameter in the central regions ($d \lesssim 4''$) is $U \sim 10^{-3}$, while at larger distances $U \gtrsim 10^{-2}$. The interstellar radiation field in the FUV band G is also strong, with a flat radially median profile and intensities around $G/G_0 \sim 10^{1.5}$, while G reaches its peak in Regions A and B ($G/G_0 \sim 10^3$).

• The visual extinction is very high, i.e. $\langle A_V \rangle \gtrsim 3$, with A_V in some spaxels exceeding 5-7 mag. These high extinctions are especially found on a region forming a ring around the center of the galaxy.

• The radially median profile for the metallicity is flat with slightly sub-solar values (i.e., $\log(Z/Z_\odot) \sim -0.2$). However, the Z distribution inferred in this work covers a quite large range (i.e., $-1.0 \lesssim \log(Z/Z_\odot) \lesssim 0.3$) denoting the heterogeneous morphology of He 2-10 in terms of physical properties across its extension.

• The gas density in Regions A and B reaches values up to $n \sim 10^{3.3}$ cm^{-3}. Then the radially median profile flattens

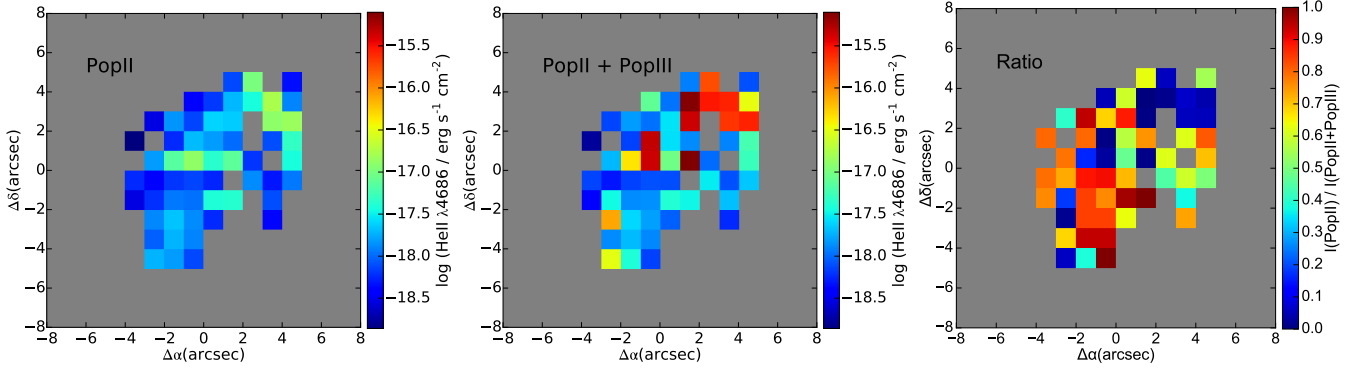**Figure 18.** Predicted HeIIλ4686 line emission by GAME for the spaxels of IZw18 using respectively the library containing only PopII stars (*left panel*), and the full library containing also the contribution from PopIII (*central panel*). *Right panel*: ratio between the predicted intensities in the *left* and *central* panels showing a negligible contribution from PopII stars in the NW region.

around a value of $n \sim 1$ cm^{-3}. Typical column densities are $N_H \sim 10^{20} - 10^{22}$ cm^{-2}.

Defining an effective scale height of the disk, as $H = N_H/n$, we obtained $0.3 \lesssim H/\text{pc} \lesssim 30$ in the central region, denoting a relatively small height of the disk. In Regions A and B we are looking at the typical dimension of Giant Molecular Clouds (GMCs), and we found high values of densities and metallicities, together with high Hα and FUV flux G. These evidences suggest that these regions host dense, dusty and highly star forming sites.

The main results for IZw18 are the following:

• Summing up the contribution from the analyzed spaxels, we obtained lower limits for the Star Formation Rate and total gas mass respectively of $SFR \gtrsim 0.007$ M$_\odot$ yr^{-1} and $M_{gas} \sim 6.9 \times 10^6$ M$_\odot$. The total gas mass of IZw18 has also been estimated by Schneider et al. (2016) who found $M_{\text{tot}} = M_{\text{HI}} + M_{\text{H}_2} + M_{\text{HII}} = 9.2 \times 10^7$ M$_\odot$, with the different phases contributing approximately equal fractions to the total gas mass. A total atomic hydrogen mass of $\sim 10^8$ M$_\odot$ has been measured by Lelli et al. (2012) throughout the entire main body, with a radius of $\sim 8''$. Both these estimates encompass a region larger than that covered by our spectra; thus our estimate is a lower limit, and consistent with the column densities of $N_H = 2 \times 10^{21}$ cm^{-2} found by us and those in HI measured by Lelli et al. (2012) with a $2''$ beam. In fact, by integrating the Lelli et al. (2012) HI radial column density distribution up to $\sim 4''$ (the area covered by our spectral maps), the resulting mass is 8-30 $\times$ 10^6 M$_\odot$, slightly higher but consistent with our results for a lower limit.

• The interstellar radiation field is very intense: in the SE knot we obtained very high values for the ionization parameter as high as $U \sim 10^2$, and FUV fluxes $G/G_0 \sim 10^{3.5}$. These high values for U, are an additional indication of the underlying high ionizing flux in IZw18, given the large uncertainties associated with the ionization parameter estimates (see U18). The prominent ionizing flux in the SE knot in our maps, can be in fact associated with the presence of a clumpy HII component, consisting of numerous knots containing blue stars (Dufour et al. 1996).

• We confirmed the extreme poor metal content of IZw18: $\log(Z/Z_\odot)$ = -1.32 ± 0.01 (i.e., 12+log(O/H) = 7.37 ± 0.01, corresponding to $\sim$ 1/20 solar). In this galaxy the metallicity remains also remarkably flat: $-1.5 \lesssim \log(Z/Z_\odot) \lesssim -1.0$, with the inferred values being within a factor of three. These low metallicity correspond also to low visual extinction across the galaxy and low dust-to-gas mass ratios: $A_V \lesssim 0.20$ mag and $\mathcal{D} \sim 10^{-3.5}$, respectively.

• IZw18 presents a low gas density environment, with most of the spaxels having $\log(n/\text{cm}^{-3}) \lesssim 1$. We obtained column densities of $N_H \sim 10^{21}$ cm^{-2}.

• We verified if the extended nebular HeII λ4686 emission in the NW component of IZw18 found by Kehrig et al. (2015, 2016) could be ascribed to PopIII stars. We implemented a modified version of GAME that is able to predict, in addition to the ISM physical properties, also the value for the intensity of a given emission line (i.e., HeII λ4686). Then, we compared the predicted HeII lines with observations finding that if PopIII stars are not taken into account, the inferred intensities for the HeII line are too low compared with observed values. Therefore, PopIII stars may provide a substantial contribution to the HeII emission.

REFERENCES

Allen D. A., Wright A. E., Goss W. M., 1976, MNRAS, 177, 91
Allende Prieto C., Lambert D. L., Asplund M., 2001, ApJ, 556, L63
Aloisi A., Tosi M., Greggio L., 1999, AJ, 118, 302

Aloisi A., et al., 2007, ApJ, 667, L151

Arp H., 1965, ApJ, 142, 402

Asplund M., Grevesse N., Sauval A. J., Allende Prieto C., Kiselman D., 2004, A&A, 417, 751

Baas F., Israel F. P., Koornneef J., 1994, A&A, 284, 403

Bacon R., et al., 2010, in Ground-based and Airborne Instrumentation for Astronomy III. p. 773508, doi:10.1117/12.856027

Baldwin J. A., Phillips M. M., Terlevich R., 1981, PASP, 93, 5

Bayet E., Gerin M., Phillips T. G., Contursi A., 2004, A&A, 427, 45

Berg D. A., et al., 2012, ApJ, 754, 98

Bian F., Kewley L. J., Dopita M. A., Juneau S., 2016, ApJ, 822, 62

Bian F., Kewley L. J., Dopita M. A., Blanc G. A., 2017, ApJ, 834, 51

Bian F., Kewley L. J., Dopita M. A., 2018, ApJ, 859, 175

Bouchet P., Lequeux J., Maurice E., Prevot L., Prevot-Burnichon M. L., 1985, A&A, 149, 330

Cabanac R. A., Vanzi L., Sauvage M., 2005, ApJ, 631, 252

Calzetti D., 2008, in Knapen J. H., Mahoney T. J., Vazdekis A., eds, Astronomical Society of the Pacific Conference Series Vol. 390, Pathways Through an Eclectic Universe. p. 121 (arXiv:0707.0467)

Calzetti D., et al., 2007, ApJ, 666, 870

Cardelli J. A., Clayton G. C., Mathis J. S., 1989, ApJ, 345, 245

Conti P. S., 1991, ApJ, 377, 115

Contreras Ramos R., et al., 2011, ApJ, 739, 74

Corbin M. R., Korista K. T., Vacca W. D., 1993, AJ, 105, 1313

Cresci G., Vanzi L., Sauvage M., Santangelo G., van der Werf P., 2010, A&A, 520, A82

Cresci G., et al., 2015, A&A, 582, A63

Cresci G., Vanzi L., Telles E., Lanzuisi G., Brusa M., Mingozzi M., Sauvage M., Johnson K., 2017, preprint, (arXiv:1704.08367)

Curti M., Cresci G., Mannucci F., Marconi A., Maiolino R., Esposito S., 2017, MNRAS, 465, 1384

Davidson K., Kinman T. D., Friedman S. D., 1989, AJ, 97, 1591

Dodorico S., Rosa M., Wampler E. J., 1983, A&AS, 53, 97

Dopita M. A., Kewley L. J., Sutherland R. S., Nicholls D. C., 2016, Ap&SS, 361, 61

Dufour R. J., Garnett D. R., Shields G. A., 1988, ApJ, 332, 752

Dufour R. J., Garnett D. R., Skillman E. D., Shields G. A., 1996, in Benvenuti P., Macchetto F. D., Schreier E. J., eds, Science with the Hubble Space Telescope - II. p. 348

Engelbracht C. W., Gordon K. D., Rieke G. H., Werner M. W., Dale D. A., Latter W. B., 2005, ApJ, 628, L29

Esteban C., García-Rojas J., Carigi L., Peimbert M., Bresolin F., López-Sánchez A. R., Mesa-Delgado A., 2014, MNRAS, 443, 624

Ferland G. J., et al., 2013, Rev. Mex. Astron. Astrofis., 49, 137

Fisher D. B., et al., 2014, Nature, 505, 186

Garland C. A., Pisano D. J., Mac Low M.-M., Kreckel K., Rabidoux K., Guzmán R., 2015, ApJ, 807, 134

Garnett D. R., Kennicutt Jr. R. C., Bresolin F., 2004, ApJ, 607, L21

Gordon K. D., Clayton G. C., Misselt K. A., Landolt A. U., Wolff M. J., 2003, ApJ, 594, 279

Gorenstein P., 1975, ApJ, 198, 95

Güver T., Özel F., 2009, MNRAS, 400, 2050

Habing H. J., 1968, Bull. Astron. Inst. Netherlands, 19, 421

Haro G., 1956, Boletin de los Observatorios Tonantzintla y Tacubaya, 2, 8

Hazard C., 1986, in Kunth D., Thuan T. X., Tran Thanh Van J., Lequeux J., Audouze J., eds, Star-forming Dwarf Galaxies and Related Objects. pp 9–29

Hirschauer A. S., et al., 2016, ApJ, 822, 108

Hunt L. K., Dyer K. K., Thuan T. X., 2005, A&A, 436, 837

Izotov Y. I., Thuan T. X., 1999, ApJ, 511, 639

Izotov I. I., Guseva N. G., Lipovetskii V. A., Kniazev A. I., Stepanian J. A., 1990, Nature, 343, 238

Izotov Y. I., Lipovetsky V. A., Chaffee F. H., Foltz C. B., Guseva N. G., Kniazev A. Y., 1997, ApJ, 476, 698

Izotov Y. I., Chaffee F. H., Foltz C. B., Green R. F., Guseva N. G., Thuan T. X., 1999, ApJ, 527, 757

Izotov Y. I., Thuan T. X., Guseva N. G., 2005, ApJ, 632, 210

Izotov Y. I., Guseva N. G., Fricke K. J., Papaderos P., 2009, A&A, 503, 61

Johnson K. E., Kobulnicky H. A., 2003, ApJ, 597, 923

Johnson K. E., Brogan C. L., Indebetouw R., Testi L., Wilner D. J., Reines A. E., Chen C.-H. R., Vanzi L., 2017, preprint, (arXiv:1712.02791)

Kauffmann G., et al., 2003, MNRAS, 346, 1055

Kawara K., Nishida M., Taniguchi Y., Jugaku J., 1987, PASP, 99, 512

Kawara K., Nishida M., Phillips M. M., 1989, ApJ, 337, 230

Kehrig C., et al., 2013, MNRAS, 432, 2731

Kehrig C., Vílchez J. M., Pérez-Montero E., Iglesias-Páramo J., Brinchmann J., Kunth D., Durret F., Bayo F. M., 2015, ApJ, 801, L28

Kehrig C., et al., 2016, MNRAS, 459, 2992

Kennicutt Jr. R. C., 1998, ApJ, 498, 541

Kennicutt R. C., Evans N. J., 2012, ARA&A, 50, 531

Kennicutt Jr. R. C., Bresolin F., Garnett D. R., 2003, ApJ, 591, 801

Kewley L. J., Dopita M. A., 2002, ApJS, 142, 35

Kewley L. J., Ellison S. L., 2008, ApJ, 681, 1183

Kewley L. J., Dopita M. A., Sutherland R. S., Heisler C. A., Trevena J., 2001, ApJ, 556, 121

Kewley L. J., Groves B., Kauffmann G., Heckman T., 2006, MNRAS, 372, 961

Kobulnicky H. A., Johnson K. E., 1999, ApJ, 527, 154

Kobulnicky H. A., Martin C. L., 2010, ApJ, 718, 724

Kobulnicky H. A., Dickey J. M., Sargent A. I., Hogg D. E., Conti P. S., 1995, AJ, 110, 116

Krumholz M. R., Dekel A., McKee C. F., 2012, ApJ, 745, 69

Kuiper G. P., 1938, ApJ, 88, 472

Kunth D., Östlin G., 2000, A&ARv, 10, 1

Kunth D., Sargent W. L. W., 1986, ApJ, 300, 496

Lebouteiller V., Heap S., Hubeny I., Kunth D., 2013, A&A, 553, A16

Lebouteiller V., et al., 2017, A&A, 602, A45

Legrand F., 2000, A&A, 354, 504

Legrand F., Kunth D., Roy J.-R., Mas-Hesse J. M., Walsh J. R., 2000, A&A, 355, 891

Lelli F., Verheijen M., Fraternali F., Sancisi R., 2012, A&A, 537, A72

Lequeux J., Peimbert M., Rayo J. F., Serrano A., Torres-Peimbert S., 1979, A&A, 80, 155

Mac Low M.-M., Ferrara A., 1999, ApJ, 513, 142

Marconi A., Risaliti G., Gilli R., Hunt L. K., Maiolino R., Salvati M., 2004, MNRAS, 351, 169

Markarian B. E., 1967, Astrofizika, 3, 24

Martin C. L., 1996, ApJ, 465, 680

Martín-Hernández N. L., Schaerer D., Peeters E., Tielens A. G. G. M., Sauvage M., 2006, A&A, 455, 853

McQuinn K. B. W., et al., 2015, ApJ, 812, 158

Meier D. S., Turner J. L., Crosthwaite L. P., Beck S. C., 2001, AJ, 121, 740

Melnick J., Terlevich R., Eggleton P. P., 1985, MNRAS, 216, 255

Méndez D. I., Esteban C., Filipović M. D., Ehle M., Haberl F., Pietsch W., Haynes R. F., 1999, A&A, 349, 801

Nguyen D. D., Seth A. C., Reines A. E., den Brok M., Sand D., McLeod B., 2014, ApJ, 794, 34

Osterbrock D. E., Ferland G. J., 2006, Astrophysics of gaseous nebulae and active galactic nuclei

Pagel B. E. J., Simonson E. A., Terlevich R. J., Edmunds M. G., 1992, MNRAS, 255, 325

Péquignot D., 2008, A&A, 478, 371

Predehl P., Schmitt J. H. M. M., 1995, A&A, 293, 889

Prevot M. L., Lequeux J., Prevot L., Maurice E., Rocca-Volmerange B., 1984, A&A, 132, 389

Pustilnik S. A., Kniazev A. Y., Pramskij A. G., 2005, A&A, 443, 91

Raiter A., Schaerer D., Fosbury R. A. E., 2010, A&A, 523, A64

Recchi S., Matteucci F., D'Ercole A., Tosi M., 2004, A&A, 426, 37

Reina C., Tarenghi M., 1973, A&A, 26, 257

Reines A. E., Deller A. T., 2012, ApJ, 750, L24

Reines A. E., Sivakoff G. R., Johnson K. E., Brogan C. L., 2011, Nature, 470, 66

Reines A. E., Reynolds M. T., Miller J. M., Sivakoff G. R., Greene J. E., Hickox R. C., Johnson K. E., 2016, ApJ, 830, L35

Roth M. M., et al., 2005, PASP, 117, 620

Roth M. M., et al., 2010, in High Energy, Optical, and Infrared Detectors for Astronomy IV. p. 774209, doi:10.1117/12.856936

Salaris M., Cassisi S., 2005, Evolution of Stars and Stellar Populations

Sánchez S. F., et al., 2017, MNRAS, 469, 2121

Santangelo G., Testi L., Gregorini L., Leurini S., Vanzi L., Walmsley C. M., Wilner D. J., 2009, A&A, 501, 495

Sargent W. L. W., Searle L., 1970, ApJ, 162, L155

Schaerer D., 2002, A&A, 382, 28

Schmidt M., 1959, ApJ, 129, 243

Schneider R., Hunt L., Valiante R., 2016, MNRAS, 457, 1842

Searle L., Sargent W. L. W., 1972, ApJ, 173, 25

Searle L., Sargent W. L. W., Bagnuolo W. G., 1973, ApJ, 179, 427

Skillman E. D., Kennicutt Jr. R. C., 1993, ApJ, 411, 655

Skillman E. D., et al., 2013, AJ, 146, 3

Stasińska G., 2002, in Henney W. J., Franco J., Martos M., eds, Revista Mexicana de Astronomia y Astrofisica Conference Series Vol. 12, Revista Mexicana de Astronomia y Astrofisica Conference Series. pp 62–69 (arXiv:astro-ph/0102403)

Terlevich R., Melnick J., Masegosa J., Moles M., Copetti M. V. F., 1991, A&AS, 91, 285

Tolstoy E., Hill V., Tosi M., 2009, ARA&A, 47, 371

Tully R. B., et al., 2013, AJ, 146, 86

Ucci G., Ferrara A., Gallerani S., Pallottini A., 2017, MNRAS, 465, 1144

Ucci G., Ferrara A., Pallottini A., Gallerani S., 2018, MNRAS, 477, 1484

Vacca W. D., Conti P. S., 1992, ApJ, 401, 543

Vacca W. D., Johnson K. E., Conti P. S., 2002, AJ, 123, 772

Vanzi L., Rieke G. H., 1997, ApJ, 479, 694

Vanzi L., Combes F., Rubio M., Kunth D., 2009, A&A, 496, 677

Vasudevan R. V., Fabian A. C., 2009, MNRAS, 392, 1124

Vílchez J. M., Iglesias-Páramo J., 1998, ApJ, 508, 248

Watson D., 2011, A&A, 533, A16

Zhu H., Tian W., Li A., Zhang M., 2017, MNRAS, 471, 3494

Zwicky F., 1965, ApJ, 142, 1293

Zwicky F., 1966, ApJ, 143, 192

van Zee L., Westpfahl D., Haynes M. P., Salzer J. J., 1998, AJ, 115, 1000

APPENDIX A: PHOTON FLUX IN HE 2-10 IS STAR-FORMING DOMINATED

In order to investigate the nature of the dominant radiation source, it is possible to use the Baldwin, Phillips & Terlevich (BPT) diagram (Baldwin et al. 1981), used to distinguish

between star-forming regions and active galactic nuclei. The analysis in this section closely follows the one presented in Cresci et al. (2017) (i.e., their Fig. 5), but here we also show the applicability of GAME to He 2-10 and with slightly different arguments how the stellar component dominates the radiation field in the galaxy. The BPT diagram makes use of two pairs of lines close in wavelength in order to minimize the effects of dust and continuum subtraction uncertainties. The line ratios involved in the BPT diagram are usually the [N II]/Hα ratio, primarily sensitive[10] to the shape of the ionizing spectrum just above 1 Rydberg, and the [O III]/Hβ ratio that probes the 1-3 Rydberg range.

The BPT diagram for the models within the GAME library (U18) and the spaxels in He 2-10 are respectively shown in the upper and lower left panels in Fig. A1. Here, we report three zones (Kewley et al. 2001; Kauffmann et al. 2003; Kewley et al. 2006): (a) regions dominated by star formation, (b) intermediate regions, (c) AGNs. Star forming regions are below the Kauffmann et al. (2003) line (black solid line in Fig. A1):

$$\log([OIII]/H\beta) = \frac{0.61}{\log([NII]/H\alpha) - 0.05} + 1.3. \quad (A1)$$

Intermediate regions fall between this and the Kewley et al. (2001) line (dashed line in Fig. A1):

$$\log([OIII]/H\beta) = \frac{0.61}{\log([NII]/H\alpha) - 0.47} + 1.19. \quad (A2)$$

Regions dominated by AGN contribution are above the two lines. In the right panel of Fig. A1, we marked these three zones with different colours. The map results to be dominated by green dots (i.e., more than 95% of spaxels), meaning that almost all the line emitting gas is ionized by young stars. This result confirms the assumption that the models contained within the library used by GAME (i.e., photoionization models coming only from stars without X-ray sources or AGNs, U18) can be applied to this galaxy.

In order to further validate this result we started from the radiation energy density of the stars contained within the galaxy, assumed to be a uniformly emitting sphere of radius r:

$$u = \frac{L_*}{4\pi r^2 c}, \quad (A3)$$

where $L_* = \epsilon M_*$ is the luminosity produced by the stars inside the galaxy, M_* is the total stellar mass contained in the galaxy, and ϵ the conversion between the stellar mass itself and the luminosity ($L_\odot M_\odot^{-1}$). By considering the previous estimates for the stellar mass contained in He 2-10 $M_* = 10^9$ M$_\odot$ (Reines et al. 2011; Nguyen et al. 2014) and a conservative value based on the mass-luminosity relation for a sub-solar mass of $\epsilon = 0.1$ $L_\odot M_\odot^{-1}$ (Kuiper 1938; Salaris & Cassisi 2005), we obtained $L_* = 10^8$ L$_\odot$. We further computed the distance d at which the radiation energy density

---

[10] The BPT lines are also sensitive to the ionization parameter, N and O abundances, and density- vs ionization-bounded HII regions.
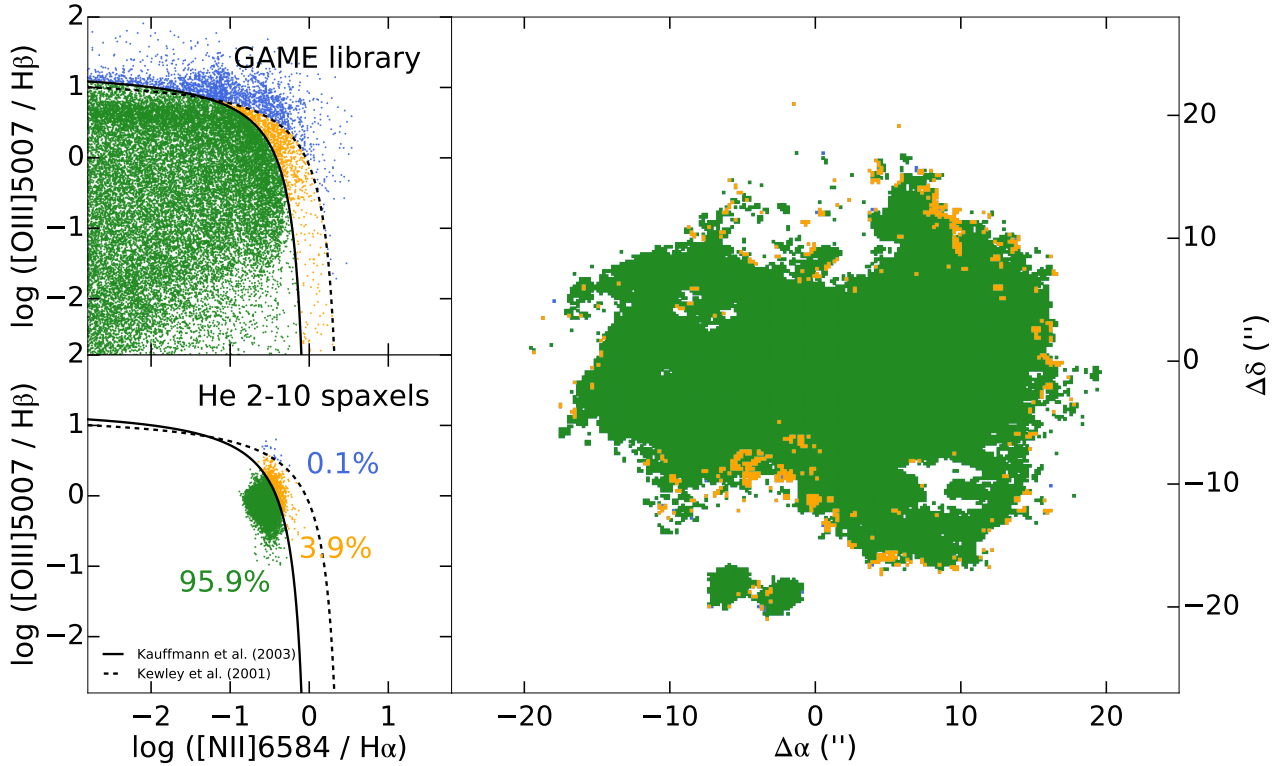
Figure A1. *Upper left panel*: BPT diagram for the models contained within the library of synthetic models of GAME. As expected, because the assumed input spectra are stellar, nearly all the models falls within the Star-Forming region. *Lower left panel*: BPT diagram for the observed spaxels of He 2-10 where we also added the percentages of the different region in the observed line ratios. *Right panel*: Map for He 2-10 color-coded based on the BPT diagram. In green are reported the spaxels having line ratios below the line reported in Kauffmann et al. (2003) denoting regions dominated by star formation.

of the stars is equal to that produced by the X-ray source by simply imposing:

$$\frac{L_X}{4\pi d^2 c} = \frac{L_*}{4\pi R^2 c}, \tag{A4}$$

where L_X is the luminosity of the X-ray source and R is the radius of the uniformly emitting sphere, that we assumed to be $R = 6'' = 240$ pc, based on the effective radius of the inner component of the galaxy provided by Nguyen et al. (2014). Given the recent estimate of $L_X \approx 10^{38}$ erg s^{-1} of Reines et al. (2016), we obtain that d $\sim$ 4 pc. Of course more realistic values (i.e., greater values) for ϵ due to young massive stars and the application of bolometric corrections (Marconi et al. 2004) for L_X up to $\sim$ 10 (e.g., Vasudevan & Fabian 2009) mean that the distance d could remain the same or become even smaller (if one assumes $\epsilon \sim 1$). The region where the energy density of the X source is relevant is very small compared to the effective radius of the galaxy. The galaxy radiation field is therefore completely dominated by the stellar component. This confirm both the results by Cresci et al. (2017) and guaranteeing the applicability of GAME to this source.

APPENDIX B: MAPS OF UNCERTAINTIES FOR HE 2-10

GAME determines 10,000 different values of each physical property (U18). The associated uncertainties are given by the standard deviations of these 10,000 realizations.

Fig. B1 shows the relative uncertainties on the He 2-10 physical properties derived directly by game and reported in Fig. 2. The typical uncertainties in the central region of the galaxy (within $\sim 10''$ from the center) are smaller than 30%, while in the case of the metallicity the vast majority of spaxels have lower uncertainties even at larger distances. The highest uncertainties remains associated to the ionization parameter U, although in the central part of the galaxy, $\sigma[\log(U)]/\log(U)$ reduces to values $\lesssim 10\%$.

APPENDIX C: GAS-TO-EXTINCTION RATIO

In this section, as an additional check of consistency for GAME, we also study the recovered gas-to-extinction ratio inside the two galaxies.

In the Galaxy, the extinction in the optical band (A_V) and the hydrogen column density (N_H) are related by the following expression (Reina & Tarenghi 1973; Gorenstein 1975;
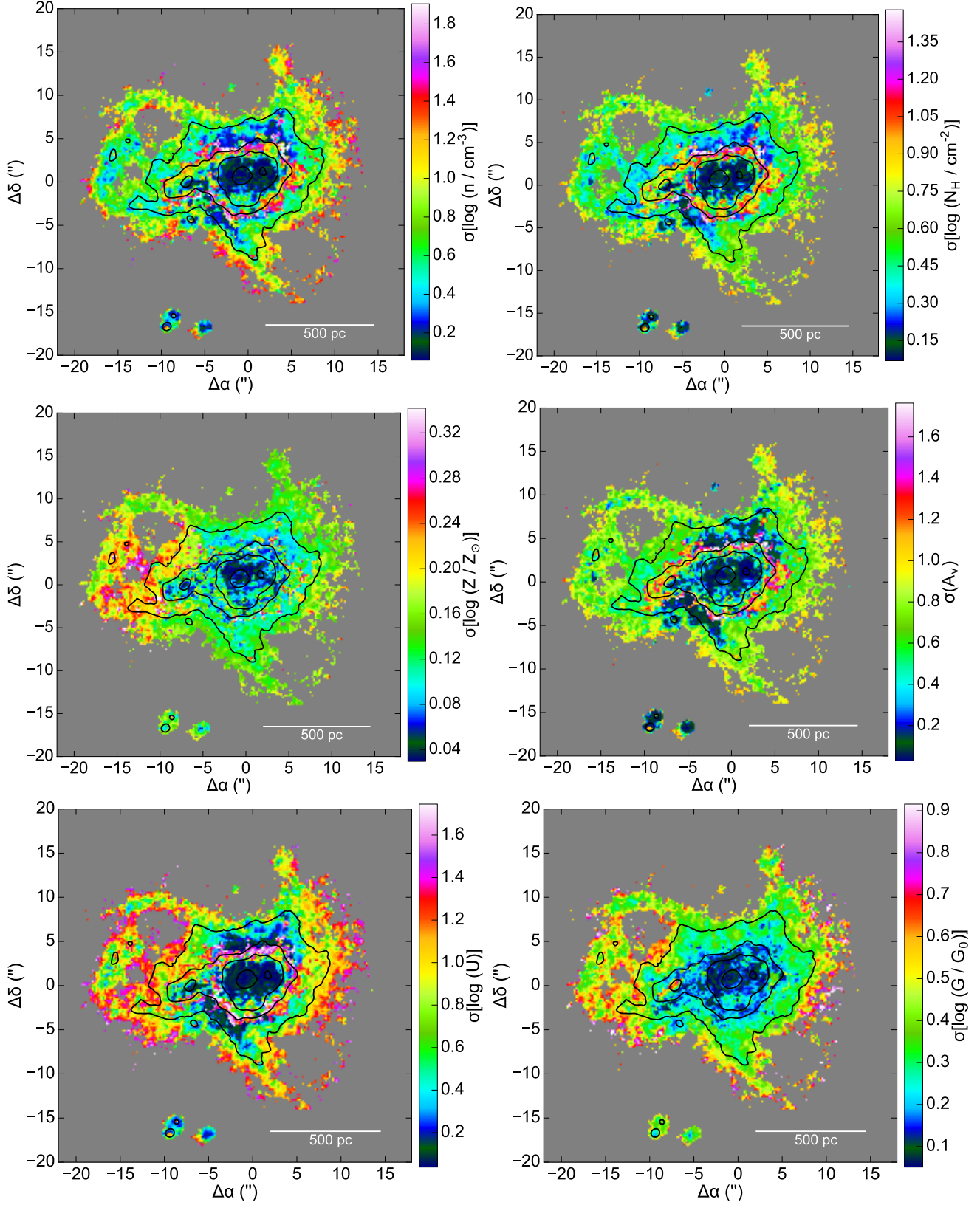
Figure B1. Relative uncertainties on the He 2-10 ISM physical properties reported in Fig. 2: density (n), column density (N_H), metallicity (Z), visual extinction (A_V), ionization parameter (U) and the FUV flux in the Habing band (G/G_0). As in Fig. 1, black lines show the contours of the Hα emission (80, 10, 4, and 1 in units of 10^{-16} ergs s^{-1} cm^{-2}). In the upper left corner we report the average relative uncertainty on the inferred values.

Predehl & Schmitt 1995; Güver & Özel 2009; Watson 2011; Zhu et al. 2017):

$$A_V = \frac{N_H}{\alpha_{MW}} \approx \frac{N_H}{2.21 \times 10^{21}\,\text{cm}^{-2}}\,\text{mag.} \tag{C1}$$

where α_{MW} is the Milky Way hydrogen-to-extinction ratio. In the GAME library we assumed instead the following functional form:

$$A_V = \frac{1}{\alpha} N_H\, Z\,. \tag{C2}$$

where $\alpha = 2.52 \times 10^{21}$ cm^{-2} mag^{-1}. To asses the GAME performances, we use our results on A_V, N_H, and Z inferred by GAME (discussed in Sec. 3 and 4). The red lines in Fig. C1, represent the best fit of eq. C2 to the GAME results. For He 2-10 and IZw18, we find $\alpha_{He2-10} = (2.40 \pm 0.02) \times 10^{21}$ cm^{-2} mag^{-1} and $\alpha_{IZw18} = 2.46^{+0.43}_{-0.37} \times 10^{21}$ cm^{-2} mag^{-1}, respectively. The α coefficients are compatible, implying that GAME is able to recover in a consistent way internal relations within the library in spite of the fact that the physical properties are recovered independently.

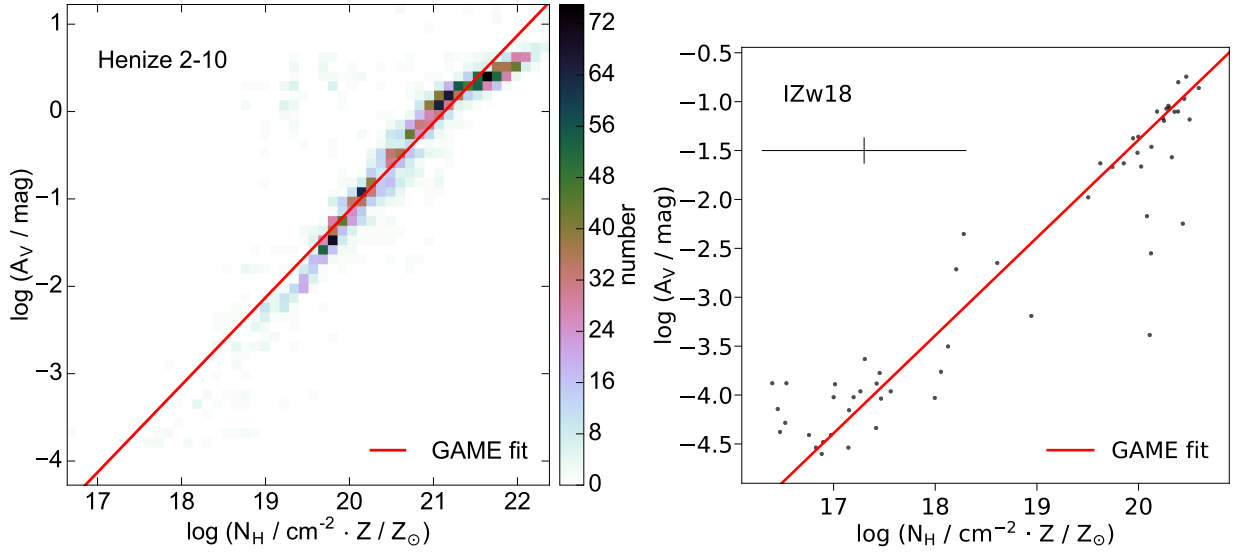This paper has been typeset from a TEX/LATEX file prepared by the author.

Figure C1. *Left panel:* 2d histogram for the visual extinction A_V as a function of the product $N_H Z$ for all the analyzed spaxels in He 2-10. The vast majority of points are located around the line. *Right panel:* visual extinction A_V as a function of the product $N_H Z$ for the analyzed spaxels in IZw18. Red lines denote the fit to the data using eq. C2. The upper-left cross denotes the typical error bar on the points.